Segregation, Finite Time Elastic Singularities and Coarsening in Renewable Active Matter

Ayan Roychowdhury, Saptarshi Dasgupta, and Madan Rao
Simons Centre for the Study of Living Machines,
National Centre for Biological Sciences-TIFR, Bengaluru, India 560065.

Material renewability in active living systems, such as in cells and tissues, can drive the large-scale patterning of forces, with distinctive phenotypic consequences. This is especially significant in the cell cytoskeleton, where multiple species of myosin bound to actin, apply contractile stresses and undergo continual turnover, that result in patterned force channeling. Here we study the dynamical patterning of stresses that emerge in a hydrodynamic model of a renewable active actomyosin elastomer comprising two myosin species. We find that a uniform active contractile elastomer spontaneously segregates into spinodal stress patterns, followed by a finite-time collapse into tension carrying singular structures that display self-similar scaling and caustics. These singular structures move and merge, and gradually result in a slow coarsening dynamics in one dimension. In addition, the nonreciprocal nature of the underlying dynamics gives rise to exceptional points that are associated with a variety of travelling states – from peristalsis to swap and trains of regular and singular stress patterns, that may coexist with each other. Both the novel segregation and excitability are consequences of time reversal symmetry breaking of the underlying active dynamics. We discuss the implications of our findings to the emergence of stress fibers and the spatial patterning of myosin.

I. INTRODUCTION

Since actomyosin is the primary agency of cell and tissue scale forces, its patterning along system spanning stress fibers [1], cables or arcs [2, 3] reveals the patterning of forces along tension chains. The cytoskeleton represent a class of active matter called *renewable active matter*; material renewability being a distinctive feature of living materials that leads to unusual mechanical responses [4] and system spanning force channeling [5]. Here we study the nature of dynamical force patterning using a hydrodynamic model of a renewable active material.

The actomyosin cytoskeleton is put together by the nonequilibrium self-assembly of a variety of crosslinkers and myosin species, that both exert and sense forces, the latter via their strain dependent turnover [6–11]. We will refer to these units of mechanotransduction as *stresslets*; the spatiotemporal patterning of these stresslets mark the patterning of forces. High resolution microscopy reveals that distinct actomyosin stress fibres [2, 3, 5, 12–14], are associated with different stresslet species displaying different cellular localisations [14, 15]. *In vivo*, these structures often coexist with persistent waves of oscillation of actomyosin, reminiscent of an excitable system [3, 16–19].

In this paper, we explore the unusual features of such renewable active matter, whose material renormalization, segregation and pattern formation, can be ultimately traced to the violation of time reversal symmetry (TRS) of the underlying active dynamics. To see this, we construct active hydrodynamic equations [20] for a mixture of contractile stresslets, such as myosin IIA and IIB [12, 14, 21, 22], on an actin elastomer, while allowing turnover of myosin stresslets [18, 23, 24]. We first show that a straightforward material consequence of TRS breaking is a renormalization of the elastic moduli that can in principle drive the material to elastic marginality [4]. We next find that a slight difference between the contractile activities or turnover rates of the stresslets, can drive spontaneous segregation, *even in the absence of any attractive interaction* – the myosin species with higher contractile activity tend to cluster together (a similar analysis for a single myosin species, leads to a segregation into myosin-rich and myosin-poor regions [25]). However, unlike conventional segregation driven by gradients in chemical potential [26], the spontaneous segregation instability of the myosin stresslets is driven by an effective elastic stress relaxation. At later times, the growing segregated domains collapse into well separated, singular structures of enhanced contractility (tensile "stress fibers"), in striking departure from conventional coarsening. We derive scaling forms for these finite time singular structures [27] and verify them with careful numerics in 1D. The amplification of contractile stresses in the singular tension structures recalls the study in [28]. These singular tension structures can be static or moving [5] and we determine the conditions for these. The moving singular tension structures merge over time and exhibit a slow coarsening dynamics at late times. In addition, renewable active materials exhibit spontaneous mechanical excitability – we find that the TRS violating hydrodynamic equations lead to a non-Hermitian dynamical matrix which exhibits nonreciprocal features [29] such as exceptional points [30] which presage the appearance of excitable travelling wave [31] and standing wave (swap) phases [29]. These excitable phases can form long-lived transients that eventually resolve into segregated singular tension structures. We leave a detailed analysis of this novel form of coexistence of nonequilibrium phases for a future study. We end with a summary of our main results and a discussion on the implications of active material renewability to evolution and physical learning. Details of the derivation of the hydrodynamic equations, linear stability analysis and dispersion curves,

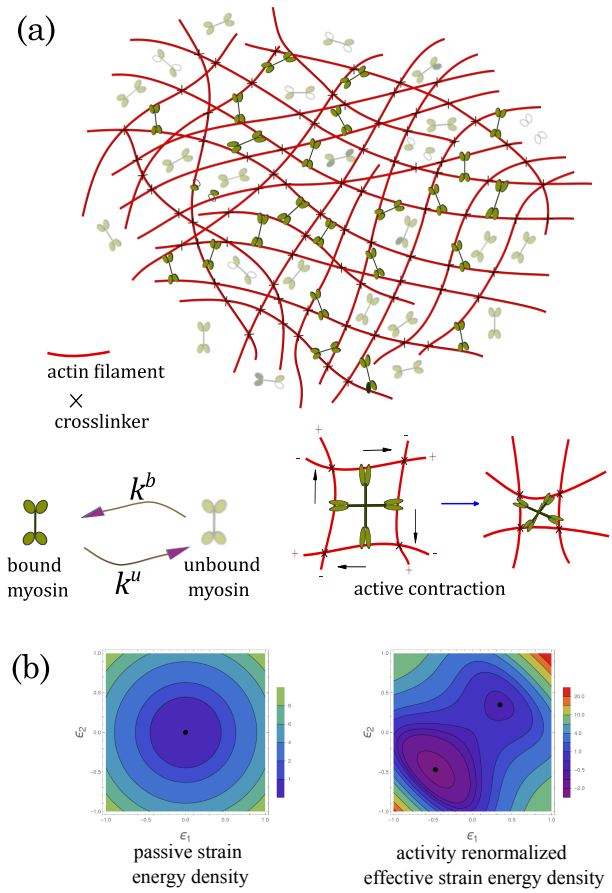

FIG. 1. **Actomyosin cytoskeleton as renewable active matter.** (a) (*top*) Schematic of the actin elastomer with crosslinkers that give it rigidity, together with bound/unbound Myo-II minifilaments. (*bottom left*) Transitions from bound to unbound Myo-II and vice versa occur with rates k_u and k_b, respectively. (*bottom right*) Bound Myo-II applies contractile stresses on the actin meshwork as shown. (b) (*left*) Elastic energy contour in the space of principal strains $\epsilon_{1,2}$ for the passive elastomer showing linear elastic behaviour with a single energy minimum (black point). (*right*) Contours of the effective elastic energy $w(\boldsymbol{\epsilon}) = \int_0^{\boldsymbol{\epsilon}} \boldsymbol{\sigma}(\boldsymbol{\epsilon}') \cdot d\boldsymbol{\epsilon}'$ renormalized by activity. Activity generates additional minima and nonlinear stabilization [4, 18].

finite time scaling and convergence analysis, and Movie captions are presented in the Appendix.

II. HYDRODYNAMIC DESCRIPTION OF ACTOMYOSIN CYTOSKELETON

We work with a crosslinked actin elastomer of mass density ρ_a, embedded in the cytosol, described by a linearized strain tensor $\boldsymbol{\epsilon} := (\nabla \boldsymbol{u} + \nabla \boldsymbol{u}^T)/2$, where $\boldsymbol{u}$ represents the displacement relative to an unstrained reference state. The hydrodynamic linear momentum balance of the overdamped elastomer is $\Gamma\, \dot{\boldsymbol{u}} = \nabla \cdot \boldsymbol{\sigma}$, where Γ is the friction of the elastomer with respect to the fluidic cytosol (whose dynamics we neglect since the volume fraction of the mesh is high), and $\boldsymbol{\sigma}(\boldsymbol{\epsilon}, \rho_a, \{\rho_i\})$ is the total stress in the elastomer, which depends on the strain $\boldsymbol{\epsilon}$, the density of the actin mesh ρ_a, and the densities ρ_i of the ith species of active bound myosin (stresslets).

The total stress $\boldsymbol{\sigma}$ is the summation of elastic stress $\boldsymbol{\sigma}^e$, the viscous stress $\boldsymbol{\sigma}^d$, and active stress $\boldsymbol{\sigma}^a$: $\boldsymbol{\sigma} = \boldsymbol{\sigma}^e + \boldsymbol{\sigma}^d + \boldsymbol{\sigma}^a$ [18, 23, 24]. The elastic stress $\boldsymbol{\sigma}^e = \frac{\delta F}{\delta \boldsymbol{\epsilon}}$ is computed from a free-energy functional $F[\boldsymbol{\epsilon}, \rho_a] = \int d\mathbf{r} f_B$, describing an isotropic elastomer, $f_B = \frac{B}{2}\epsilon^2 + \mu|\tilde{\boldsymbol{\epsilon}}|^2 + C\,\delta\rho_a\,\epsilon + \frac{A}{2}\delta\rho_a^2$, where $\epsilon := \mathrm{tr}\boldsymbol{\epsilon}$ is the dilational strain and $\tilde{\boldsymbol{\epsilon}} := \boldsymbol{\epsilon} - (\epsilon/d)\mathbf{I}$ is the deviatoric strain, $B > 0$ and $\mu > 0$ are the passive elastic bulk and shear moduli, respectively, $\delta\rho_a := \rho_a - \rho_a^0$ is the local deviation of ρ_a from its state value ρ_a^0, $A^{-1} > 0$ is the isothermal compressibility at constant strain, and $C > 0$ couples dilation with local density variation. The passive viscous stress of the elastomer is $\boldsymbol{\sigma}^d = \eta_b\, \dot{\epsilon}\, \mathbf{I} + 2\eta_s\, \dot{\tilde{\boldsymbol{\epsilon}}}$, where $\eta_{b,s}$ are the bulk and shear viscosities, respectively. We take the active stress $\boldsymbol{\sigma}^a$ to be isotropic and of the form: $\boldsymbol{\sigma}^a = \chi(\rho_a) \sum_i \zeta_i\, \rho_i\, \mathbf{I}$, where $\zeta_i > 0$ are activity coefficients representing contractile stress, and $\chi(\rho_a)$ is a sigmoidal function which captures the dependence of the active stress on the local actin mesh density. We will further assume that the turnover of the actin mesh is fast compared to the its stress relaxation time scale, thus enslaving the local density fluctuation $\delta\rho_a$ to the meshwork strain: $\delta\rho_a = -\frac{C}{A}\epsilon$.

The bound active stresslets exert contractile stresses and undergo turnover, which can in general be strain dependent; here we take the unbinding rates to be of the form: $k_i^u(\boldsymbol{\epsilon}) = k_{i0}^u\, e^{\alpha_i\, \epsilon}$, where $k_{i0}^u > 0$, are the strain independent parts of the respective rates, and α_i are dimensionless numbers; $\alpha_i > 0$ represent *catch bonds* where local contraction (extension) will decrease (increase) the unbinding rate of the stresslets, while $\alpha_i < 0$ represent *slip bonds* where local extension (contraction) will decrease (increase) the unbinding rate of the stresslets [6–8, 18].

For a binary mixture of stresslets, the physics of segregation and the subsequent force patterning is explored by casting the hydrodynamic equations in terms of the average density $\rho := (\rho_1 + \rho_2)/2$, and relative density $\phi := (\rho_1 - \rho_2)/2$ (ρ_1 is the more contractile species):

$$\dot{\boldsymbol{u}} = \nabla \cdot \boldsymbol{\sigma}, \tag{1a}$$

$$\dot{\rho} + \nabla \cdot (\rho\, \dot{\boldsymbol{u}}) = D\nabla^2\rho + 1 - \frac{C\,\epsilon}{A} - k_{\mathrm{avg}}^u\, \rho - k_{\mathrm{rel}}^u\, \phi, \tag{1b}$$

$$\dot{\phi} + \nabla \cdot (\phi\, \dot{\boldsymbol{u}}) = D\nabla^2\phi + k_{\mathrm{rel}}^b \left(1 - \frac{C\,\epsilon}{A}\right) - k_{\mathrm{avg}}^u\, \phi - k_{\mathrm{rel}}^u\, \rho; \tag{1c}$$

made dimensionless by setting the units of time, length and density, as $t^\star := 1/k_{\mathrm{avg}}^b$, $l^\star := \sqrt{\eta_b/\Gamma}$ and ρ_a^0, where $k_{\mathrm{avg}}^{b,u} := (k_1^{b,u} + k_2^{b,u})/2$, $k_{\mathrm{rel}}^{b,u} := (k_1^{b,u} - k_2^{b,u})/2$ are the average and relative binding (unbinding) rates of the stresslets, respectively. The derivation of these equations together with the underlying assumptions are presented in Appendix A.

By Taylor expanding the function $\chi(\rho_a)$ about its state value ρ_a^0, and with $\delta\rho_a$ enslaved to ϵ, the total stress can be recast to cubic order in strain as,

$$\boldsymbol{\sigma} = \Big(\sigma_0 + \tilde{B}\,\epsilon + B_2\,\epsilon^2 + B_3\,\epsilon^3 + \eta_b\,\dot{\epsilon}\Big)\mathbf{I} + 2\mu\tilde{\boldsymbol{\epsilon}} + 2\eta_s\,\dot{\tilde{\boldsymbol{\epsilon}}} \quad (2)$$

with a purely active prestress $\sigma_0(\rho,\phi) := 2\chi(\rho_a^0)(\zeta_{\rm avg}\,\rho + \zeta_{\rm rel}\,\phi)$, where $\zeta_{\rm avg} := (\zeta_1+\zeta_2)/2 > 0$, $\zeta_{\rm rel} := (\zeta_1 - \zeta_2)/2$ are the average and relative contractility, respectively, an activity renormalized linear elastic bulk modulus $\tilde{B}(\rho,\phi) := B - \frac{C^2}{A} - 2\chi'(\rho_a^0)\,\frac{C}{A}(\zeta_{\rm avg}\,\rho + \zeta_{\rm rel}\,\phi)$ and activity generated nonlinear elastic bulk moduli $B_2(\rho,\phi), B_3(\rho,\phi)$, linearly dependent on ρ and ϕ (see Appendix A3).

The material model, described by Eqs. (1), (2), is dynamic, renewable and active, and breaks time reversal symmetry (TRS) in that it contains terms that are not derivable from a free energy. The spatiotemporally inhomogeneous material moduli $\tilde{B}(\rho,\phi)$ and $B_{2,3}(\rho,\phi)$ lead to a rich effective elastic energy landscape with multiple wells, tuned dynamically by activity and material renewal. As we explore in detail later, accumulation of the stronger contractile motors (i.e., $\rho \gg 1$, $\phi > 0$) can make $\tilde{B}(\rho,\phi) \to 0$ locally and even drive it to negative values, thus, triggering localized linear elastic instability, in which case the purely active higher order moduli $B_{2,3}$ would stabilize the nonlinear response [4].

The renormalization of elastic moduli show up in the unusual mechanical behaviour of renewable active materials [4]. Here we focus on how these dynamic material properties drive stress patterning, directly relevant to the actomyosin cytoskeleton, leading to the emergence of singular tension structures and excitability.

III. POSITIVE REINFORCEMENT BETWEEN ACTIVITY AND TURNOVER LEADS TO SEGREGATION OF STRESSLETS

As the first step towards force patterning, we discuss a novel segregation into domains of high and low contractility. This is readily seen from a linear stability analysis about the undeformed symmetric mixture ($\boldsymbol{u} = \mathbf{0}$, $\phi = 0$) described by the linear dynamical system, $\dot{\mathbf{w}} = \mathbf{M}\mathbf{w}$ (see Appendix B2), which governs the evolution of the perturbation $\mathbf{w} = \Big(\hat{\delta\epsilon}(t,\mathbf{q})\ \hat{\delta\rho}(t,\mathbf{q})\ \hat{\delta\phi}(t,\mathbf{q})\Big)^T$ that depends on the Fourier wave vector $\mathbf{q}$. Here, $\hat{\delta\epsilon} \equiv \delta\hat{u}_{\parallel} := \hat{\delta\boldsymbol{u}}\cdot\mathbf{q}$ is the Fourier transform of the dilation strain field ϵ, and the dynamical matrix is

$$\mathbf{M} = \begin{bmatrix} -\frac{(\tilde{B}+\mu)\,q^2}{1+q^2} & -\frac{2\chi(\rho_a^0)\,\zeta_{\rm avg}\,q^2}{1+q^2} & -\frac{2\chi(\rho_a^0)\,\zeta_{\rm rel}\,q^2}{1+q^2} \\ -\Big(\frac{C}{A} + \frac{k_3}{k_1} - \frac{(\tilde{B}+\mu)\,q^2}{(1+q^2)k_1}\Big) & -Dq^2 - k_1 + \frac{2\chi(\rho_a^0)\,\zeta_{\rm avg}\,q^2}{(1+q^2)k_1} & -k_2 + \frac{2\chi(\rho_a^0)\,\zeta_{\rm rel}\,q^2}{(1+q^2)k_1} \\ -\Big(\frac{k_2}{k_1}\frac{C}{A} + \frac{k_4}{k_1}\Big) & -k_2 & -Dq^2 - k_1 \end{bmatrix}, \quad (3)$$

where $q := |\mathbf{q}|$, and $\tilde{B} := B - \frac{C^2}{A} - 2\chi'(\rho_a^0)\,\frac{C}{A}\frac{\zeta_{\rm avg}}{k_1}$ is the activity renormalized bulk modulus of the homogeneous symmetric mixture. Here the turnover rates appearing in Eq. (1) have been expanded to linear order in ϵ,

$$k^u_{\rm avg}(\boldsymbol{\epsilon}) = k_1 + k_3\,\epsilon + o(|\boldsymbol{\epsilon}|), \quad (4a)$$

$$k^u_{\rm rel}(\boldsymbol{\epsilon}) = k_2 + k_4\,\epsilon + o(|\boldsymbol{\epsilon}|); \quad (4b)$$

where the parameters that appear in Eq. (3), namely

$$k_1 := \frac{k^u_{10} + k^u_{20}}{2} > 0, \quad \text{and} \quad k_2 := \frac{k^u_{10} - k^u_{20}}{2}, \quad (5)$$

represent the average and relative bare unbinding rates (i.e., strain independent), respectively, and

$$k_3 := \frac{k^u_{10}\alpha_1 + k^u_{20}\alpha_2}{2}, \quad \text{and} \quad k_4 := \frac{k^u_{10}\alpha_1 - k^u_{20}\alpha_2}{2}, \quad (6)$$

represent the coefficients of the strain dependent parts of the relative and average unbinding rates, respectively. We see that the linear dynamics of the transverse Fourier displacement mode $\delta\hat{u}_\perp := \hat{\delta\boldsymbol{u}}\cdot\mathbf{q}_\perp$ uncouples from the rest of the dynamics.

Note that $\mathbf{M}$ is non-Hermitian due to TRS breaking; as a consequence, the eigenvectors along which the perturbations propagate are no longer orthogonal to each other and may even co-align for some parameter values, as we will see later.

With the simplifying assumption that the bare rates of binding and unbinding are identical in the two myosin species, the instabilities are determined solely by the maximum eigenvalue of $\mathbf{M}$,

$$\lambda_{max} = -\frac{\lambda_a - \sqrt{\lambda_b}}{2(1+q^2)} \quad (7)$$

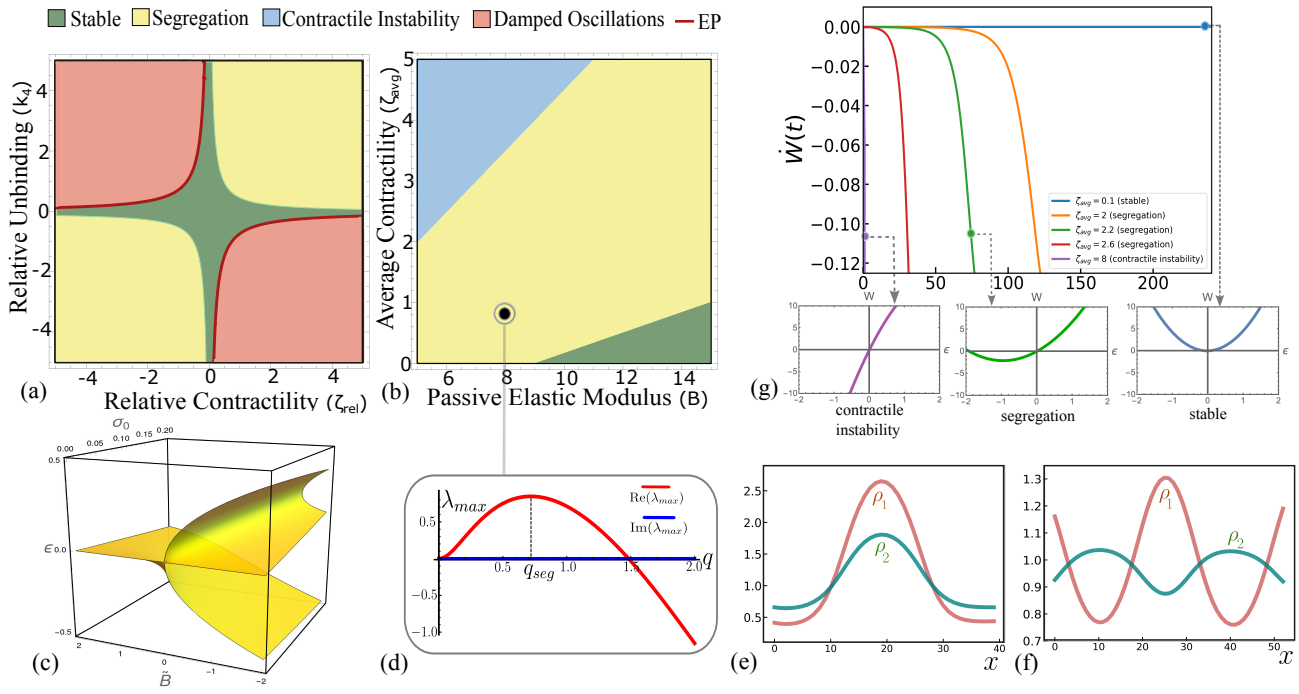

FIG. 2. **Linear stability phase diagrams and segregation instability in a binary mixture of stresslets.** (a) Phase diagram in relative unbinding versus contractility, with $B = 8$, $\zeta_{\rm avg} = 1$, shows segregation instability (yellow) for $\zeta_{\rm rel} k_4 > 0$. The red line corresponds to a line of exceptional points (EP), where the eigenvectors of the dynamical matrix $\mathbf{M}$ co-align. (b) Phase diagram in bare elastic modulus versus average contractility for $\zeta_{\rm rel} k_4 > 0$, shows transitions from the stable phase to segregation followed by elastic contractile instability, with increasing $\zeta_{\rm avg}$. (c) Graph of the minimum of the effective elastic energy at a fixed value of ρ and ϕ, i.e. $\sigma_0 + \tilde{B}\epsilon + B_2\epsilon^2 + B_3\epsilon^3 = 0$, showing the elastic instability $\tilde{B} \leq 0$ as a pitchfork bifurcation of the unstrained state into a spinodal pattern of expansion and contraction, with the active prestress σ_0 acting as an "external field". Tensile prestress $\sigma_0 > 0$ biases the stable branch towards contraction ($\epsilon < 0$). (d) Typical dispersion curve obtained from a linear analysis of the segregation instability, where q_{seg} is the fastest growing mode. (e,f) Snapshots of segregation obtained from a numerical solution of the scalar version of Eq. (1) with periodic boundary condition in 1D (see Movie 1, Movie 2). Co-localisation and separation of density peaks of the individual segregating stresselets, when (e) the two stresslets have catch bonds with $k_3 = 2$ (see Eq. (6)), and when (f) stresslet 1(2) has catch(slip) bond with $k_3 = -0.5$. The ratio ρ_1/ρ_2 within the domain depends on activity, turnover and the stress jump across the domain. We have set $C = A = D = 1$, $k_1 = 1$, $k_2 = 0$, $\chi(\rho_a^0) = 1$ and $\chi'(\rho_a^0) = 1$, $\zeta_{rel} = 1$ and $\zeta_{avg} = 2.8$ throughout. (g) Power density $\dot{W}(t)$ (see text) monotonically decreases in the linear segregation regime; the rate of decrease goes to $-\infty$ as the average activity $\zeta_{\rm avg}$ increases and the elastic instability is approached. Outsets show the minimum ϵ_{min} of the effective strain energy density w_{lin} at fixed (ρ, ϕ) moving to $-\infty$ as $\zeta_{\rm avg}$ increases (see Eq. (10)).

where

$$\lambda_a := k_1 + \left(\tilde{B} + \mu - \frac{2\chi(\rho_a^0)\zeta_{\rm avg}}{k_1} + D + k_1\right) q^2 + D\, q^4, \tag{8a}$$

$$\lambda_b := \lambda_a^2 - 4\, q^2(1+q^2)k_1^2\Bigg[(\tilde{B}+\mu)\, D\, q^2 + k_1\left(\tilde{B} + \mu - 2\chi(\rho_a^0)\left(\frac{\zeta_{\rm avg}}{k_1}\left(\frac{C}{A} + \frac{k_3}{k_1}\right) + \frac{\zeta_{\rm rel}}{k_1}\frac{k_4}{k_1}\right)\right)\Bigg]. \tag{8b}$$

With this in hand, we are in a position to describe both the elastic and segregation instabilities of the uniform elastomer driven by active stresses and turnover (Fig. 2).

Elastic (contractile) instability. Starting from a stable unstrained elastomer, we see that large enough average activity $\frac{\zeta_{\rm avg}}{k_1}$ drives the renormalized longitudinal elastic modulus $\tilde{B} + \mu$ of the symmetric mixture to negative values, leading to a linear elastic instability of the underlying elastomer [4, 18] that affects all modes $q \in [0, \infty)$ (see Fig. 2(b) and dispersion curve in Fig. B7). This elastic spinodal decomposition into patterns of positive and negative ϵ is a pithfork bifurcation, with prestress as an 'external field' controlling it (shown in Fig. 2(f)). The contracted ($\epsilon < 0$) domains eventually show up as self-penetration and subsequent collapse (halted by steric effects) of the contractile mixture, unless constrained by appropriate boundary conditions [4]. The microscopic origin of this elastic instability can be attributed to the microbuckling [28], the loss of crosslinkers, resulting in

relative sliding of the semiflexible actin filaments [32], to micro-wrinkling [33] and stretching-to-bending transition [34].

We will see that the force patterning that we discussed earlier is achieved through entrapping this contractile instability into segregated domains. In the linear theory, this segregation, and other nonequilibrium phases, show up in the mechanically stable regime of the active elastomer, $\tilde{B} + \mu > 0$.

Segregation instability. As λ_b increases beyond 0, λ_{max} goes from being negative (stable) to positive, leading to a long-wavelength instability in ϕ. The fastest growing wave-vector q_{seg} sets the characteristic width q_{seg}^{-1} of the segregated pattern (Fig. 2(c), Eq. (C1)), provided $\tilde{B}$ is bounded between,

$$0 < \tilde{B} + \mu < 2\chi(\rho_a^0)\left(\frac{\zeta_{\rm avg}}{k_1}\left(\frac{C}{A} + \frac{k_3}{k_1}\right) + \frac{\zeta_{\rm rel}}{k_1}\frac{k_4}{k_1}\right). \quad (9)$$

This linear segregation regime is typically realised when the relative activity $\zeta_{\rm rel}$ and strain dependent unbinding k_4 have the same sign, which implies $k_1^u(\epsilon) < k_2^u(\epsilon)$, since the stresslets are contractile. To drive segregation, the stresslet with stronger contractile activity must have a lower strain-dependent unbinding rate. Note that the density peaks of the individual stresslets colocalise (Fig. 2(e), Movie 1) unlike in conventional phase separation. This is reminiscent of the co-assembly of Myosin IIA and IIB during the formation of stress fibers [14, 15, 22], and occurs when both stresslets exhibit catch-bond behaviour ($\alpha_1, \alpha_2 > 0$). For slip-bond response of the weaker species ($\alpha_1 > 0$, $\alpha_2 < 0$), the individual density peaks separate (Fig. 2(f), Movie 2).

Driving force for linear segregation. Since the stresslets do not directly interact with each other, the driving force for this segregation in the linear theory must come from their indirect interaction through the elastomer strain. This is best seen by defining the activity renormalized "elastic energy density" in the linear elastic regime, as $w_{lin} = \int_0^\epsilon \sigma(\epsilon')d\epsilon' := \sigma_0(\rho,\phi)\,\epsilon + \frac{1}{2}\tilde{B}(\rho,\phi)\,\epsilon^2$. Now for any fixed value of ρ and ϕ, the minimum of w_{lin} occurs at the strain

$$\epsilon_{min} = -\frac{\sigma_0}{\tilde{B}} = -\frac{2\,\chi(\rho_a^0)\big(\zeta_{\rm avg}\,\rho + \zeta_{\rm rel}\,\phi\big)}{B - \frac{C^2}{A} - 2\,\chi'(\rho_a^0)\,\frac{C}{A}\big(\zeta_{\rm avg}\,\rho + \zeta_{\rm rel}\,\phi\big)}. \quad (10)$$

Without activity, $\epsilon_{min} = 0$. With activity and large $\zeta_{\rm rel}$ (implying segregation), σ_0 is large and $\tilde{B}$ is a small positive number; hence, ϵ_{min} becomes highly contractile. As the elastic instability is approached with further increase in activity, $\epsilon_{min} \to -\infty$ (see Fig. 2(g) insets).

We find from a 1D numerical solution in a system of size L, that the power density $\dot{W} = (1/L)\int \dot{w}_{lin}\,dx$ associated with linear segregation regime is negative (Fig. 2(g)), i.e., W is a Lyapunov functional driving segregation of the stresslets.

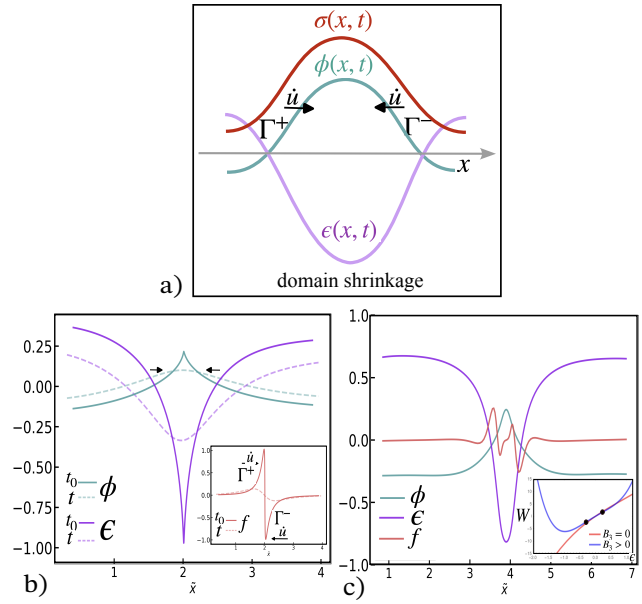

FIG. 3. **Mechanism of singularity formation.** (a) Schematic of a single domain showing the profiles of the segregation field ϕ, strain ϵ and stress σ. The magnitude of the velocities of the interfaces $\Gamma^\pm$ bounding the domain are $\dot{u}$, causing them to move towards each other as the singularity develops. (b) Snapshots from 1D numerical simulation of a single segregated domain showing the segregation parameter ϕ and strain ϵ profiles at an early time point t (dashed line) and later time point t_0 (solid line) at which the singularity develops when the steric term $B_3 = 0$. Inset shows the corresponding force $f = \partial_x\sigma$ ($\equiv \dot{u}$) that drives the velocity of the interfaces $\Gamma^\pm$ towards each other, leading to growing amplitudes of ϕ and ϵ and an eventual singularity. All plots are shown in the deformed coordinate $\tilde{x} = x + u(x,t)$. Parameters are $B = 6, \chi(\rho_a^0) = 1, \chi(\rho_a^0)' = 1, \chi(\rho_a^0)'' = 0.5, \chi(\rho_a^0)''' = 0, \zeta_{avg} = 2, \zeta_{rel} = 2$. (c) Physical resolution of the singularities in ϕ, ϵ and f, by introducing a large steric term $B_3 = 10$. (*Inset*) Comparison of the effective elastic energy landscapes for $B_3 = 0$ and $B_3 = 10$. The two black points $(-B_2 \pm \sqrt{B_2^2 - 3\tilde{B}B_3})/3B_3$, for fixed (ρ,ϕ), mark the elastic spinodals bounding the unstable regime of the energy landscape for a finite $B_3 > 0$; the spinodals move to infinity as $B_3 \to 0$. See Movie 3 for (b) and (c).

IV. FINITE-TIME ELASTIC SINGULARITIES

As time passes, nonlinear terms in the dynamical equations become prominent; the growing spinodal patterns predicted by the linear analysis, start to shrink into singular structures that carry tension. This behaviour is quite unlike the usual segregating mixture, where nonlinearities temper the exponential growth of the domains to a slower power-law growth [26].

To see this, let us focus on a single domain of the evolving spinodal pattern in 1D of width $\sim q_{seg}^{-1}$ and bounded by two interfaces $\Gamma^\pm$, Fig. 3(a). The segregation field $\phi > 0$ inside the domain and $\phi < 0$ outside. The

forces $\partial_x\sigma$ acting across this domain cause it to gradually shrink, concentrating the more contractile stresslet within. Eventually, the center of this shrinking domain enters the elastic instability regime $\partial^2_{\epsilon\epsilon}w(\epsilon;\rho,\phi) \leq 0$ when the stresslet density is large enough (Fig. 3), following which there is no escape from collapse, leading to the formation of singular force carrying structures in finite time. These singular tensile structures which harbour the more contractile stresslet, remain well separated owing to the active prestress in the surrounding elastic medium which predominantly harbours the less contractile stresslet.

In an actual physical situation, the elastic singularity is never reached and one ends up with highly concentrated tensile regions of finite width set by the constraint of steric hindrance, represented by the ϵ^3 term in the effective elastic stress (Eq. (2)), see Fig. 3(c). This is consistent with the observations [14, 15] on the segregation of the more contractile non-muscle Myosin IIA from the less contractile Myosin IIB,C.

Self-similar solution for finite-time singularity. Following the above discussion, we analyse the approach to the finite-time singularity starting from the linear segregation pattern, by dropping the steric stabilising cubic term in elastic stress and the turnover of stresslets. We also neglect the viscous stresses for convenience, though this does not pose any difficulties. The dynamical equations in 1D then reduce to the conservative system

$$\dot{\rho} = \partial_x\big(D\partial_x\rho - \partial_x\sigma\,\rho\big) \tag{11a}$$

$$\dot{\phi} = \partial_x\big(D\partial_x\phi - \partial_x\sigma\,\phi\big) \tag{11b}$$

$$\dot{\epsilon} = \partial^2_{xx}\sigma, \tag{11c}$$

where

$$\begin{aligned}\sigma = {} & 2\,\chi(\rho_a^0)\,(\zeta_{\rm avg}\,\rho + \zeta_{\rm rel}\,\phi) \\ & + \Big(B - C^2 - 2\,\chi'(\rho_a^0)\,C\big(\zeta_{\rm avg}\,\rho + \zeta_{\rm rel}\,\phi\big)\Big)\,\epsilon \\ & + \chi''(\rho_a^0)\,C^2\,\big(\zeta_{\rm avg}\,\rho + \zeta_{\rm rel}\,\phi\big)\,\epsilon^2. \end{aligned} \tag{12}$$

During the initial stages of linear segregation when ρ, ϕ and ϵ are relatively small, the first two terms (active prestress and linear elasticity) in the stress field Eq. (12) dominate. However, as ρ, ϕ and ϵ grow exponentially due to linear instability, they become large inside the segregated domains where local density is high. When this happens, the lowest order nonlinearity, the ϵ^2 term in Eq. (12) starts dominating over other terms. This dominance of a particular power of the driving field in the final approach to the singularity, is at the origin of the scale invariance of the equation, and, hence, of the solution near the singularity [27]. Note that in the relatively low density regions between the high density domains, the dominant term is the active prestress, as the effective bulk modulus in the second term in Eq. (12) is small. Thus the interface between the high and low density regions, is *pushed* by the active prestress and *pulled* by the contractile instability.

We expect that there exists a fixed space-time location (x_0, t_0) at which the the first singularity appears. The scale invariance of the solution near this singularity implies that, starting from a typical segregated domain at time $t < t_0$ as shown in Fig. 3, the height of the profiles ρ, ϕ and ϵ must grow and the domain width must shrink at $t \to t_0$, as power laws with appropriate *universal* scaling exponents. This a consequence of the fact that they arise solely from the structure of the partial differential equations, and are independent of initial conditions [27]. This motivates us to express the solution as a self-similar form,

$$\rho(x,t) = \frac{C_0}{(t_0-t)^s}R(\xi), \tag{13a}$$

$$\phi(x,t) = \frac{A_0}{(t_0-t)^p}\Phi(\xi), \tag{13b}$$

$$\epsilon(x,t) = \frac{B_0}{(t_0-t)^q}E(\xi), \tag{13c}$$

with the scaling variable, $\xi := (x-x_0)/(t_0-t)^r$. In the above, A_0, B_0 and C_0 are constants; $s>0$, $p>0$, $q>0$ and $r>0$ are the scaling exponents; and R, Φ and E are analytic scaling functions.

With these scaling forms, we are left with the following unknowns – the blowup time and location t_0, x_0, the exponents s, p, q and r, and the similarity profiles $R(\xi)$, $\Phi(\xi)$ and $E(\xi)$. These are obtained by substituting the similarity forms Eqs. (13) into the Eqs. (11). Since diffusion cannot produce any finite-time singularity, we will ignore the diffusion term in the ρ and ϕ-equations.

Since we have ignored binding-unbinding, $\rho(x,t)$ and $\phi(x,t)$ are conserved, thus

$$\int_{-L/2}^{L/2}\rho(x,t)\,dx = \int\frac{C_0}{(t_0-t)^{s-r}}R\,d\xi = const., \quad \text{and} \tag{14a}$$

$$\int_{-L/2}^{L/2}\phi(x,t)\,dx = \int\frac{A_0}{(t_0-t)^{p-r}}\Phi\,d\xi = const. \tag{14b}$$

which immediately implies $s=p=r$. To get the asymptotic form of the singularity, we analyse the coupled nonlinear ODEs written in terms of the scaling variable ξ (see Eqs. (D3), (D4) and (D5) in Appendix D) using the method of dominant balance [27]. The largest order nonlinearity (coming from the ϵ^2 term in Eq. (12)) should dominate near the singularity, and must balance the time derivative terms. Thus,

$$1+q = s+r+2q+r, \tag{15a}$$

$$1+s = s+s+r+2q+r, \tag{15b}$$

$$1+p = p+s+r+2q+r \tag{15c}$$

$$\Rightarrow\ s=p=r=\frac{1}{3},\ q=0, \tag{15d}$$

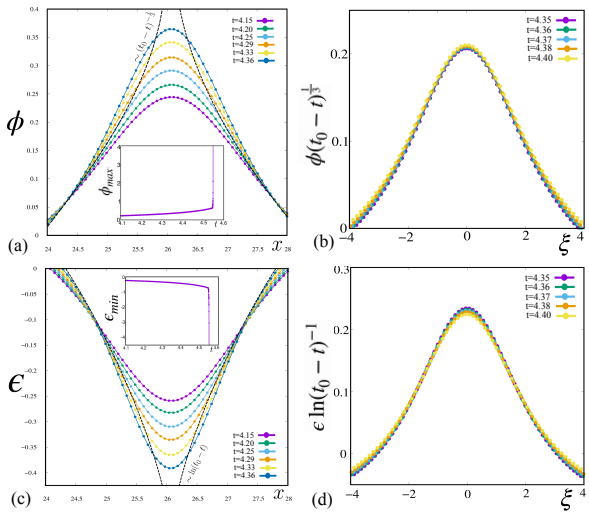

FIG. 4. **Numerical analysis of finite time singularities.** (a)-(d) Numerical results verifying the scaling profiles of ϕ and ϵ and the formation of a singularity in finite time. (b,d) show scaling collapse of the ϕ and ϵ profiles near the singularity, as predicted from theory; $\xi = (x - x_0)/(t_0 - t)^{\frac{1}{3}}$ is the scaling variable. Starting from a homogeneous unstrained symmetric state, a 1D numerical solution of Eq. (1) gives the value of the finite time blowup $t_0 = 4.55$ and blowup location $x_0 = 26.06$ (see insets in (a) and (c)).

which immediately leads to the following scaling forms,

$$\rho \sim \frac{1}{(t_0-t)^{\frac{1}{3}}} R\Big(\frac{x-x_0}{(t_0-t)^{\frac{1}{3}}}\Big), \;\; \dot{\rho} \sim \frac{1}{(t_0-t)^{\frac{4}{3}}} R_1\Big(\frac{x-x_0}{(t_0-t)^{\frac{1}{3}}}\Big), \tag{16a}$$

$$\phi \sim \frac{1}{(t_0-t)^{\frac{1}{3}}} \Phi\Big(\frac{x-x_0}{(t_0-t)^{\frac{1}{3}}}\Big), \;\; \dot{\phi} \sim \frac{1}{(t_0-t)^{\frac{4}{3}}} \Phi_1\Big(\frac{x-x_0}{(t_0-t)^{\frac{1}{3}}}\Big), \tag{16b}$$

$$\dot{\epsilon} \sim \frac{1}{t_0-t} E_1\Big(\frac{x-x_0}{(t_0-t)^{\frac{1}{3}}}\Big) \;\Rightarrow\; \epsilon \sim \ln(t_0-t) E\Big(\frac{x-x_0}{(t_0-t)^{\frac{1}{3}}}\Big). \tag{16c}$$

The initial data in ϕ is of the form $\phi(x,0) \sim \phi_0\Big(\frac{x-x_0}{l}\Big)$, parameterized by an initial width l. We obtain the blowup time t_0 using dimensional analysis: $t_0 \sim \tau(l/\ell)^3$, where $\tau := \Big(\frac{\Gamma}{B_2{}^2}\Big)^{\frac{1}{3}}$, $\ell := \Big(\frac{B_2}{\Gamma^2}\Big)^{\frac{1}{3}}$, and $B_2 := \chi''(\rho_a^0)\, C^2\, \zeta_{\rm rel}$. Thus the space-time location of the first blowup (x_0, t_0) will depend on the initial data that we determine from the numerical solution.

To obtain the scaling functions, we solve the nonlinear ODEs near the singularity

$$\big(\xi\, R\big)' = -3\chi''(\rho_a^0)\, B_0^2 \left(R \left(\big(C_0 \zeta_{\rm avg} R + A_0 \zeta_{\rm rel} \Phi\big)\, E^2 \right)' \right)' \tag{17a}$$

$$\big(\xi\, \Phi\big)' = -3\chi''(\rho_a^0)\, B_0^2 \left(\Phi \left(\big(C_0 \zeta_{\rm avg} R + A_0 \zeta_{\rm rel} \Phi\big)\, E^2 \right)' \right)', \tag{17b}$$

$$\xi\, E' = 3\chi''(\rho_a^0)\, B_0 \left(\big(C_0 \zeta_{\rm avg} R + A_0 \zeta_{\rm rel} \Phi\big)\, E^2 \right)''. \tag{17c}$$

with appropriate boundary conditions. This second order system of ODEs requires two boundary conditions each. One natural choice for the boundary conditions comes from symmetry:

$$R'(0) = \Phi'(0) = E'(0) = 0. \tag{18}$$

The other boundary conditions come from the asymptotics of the profiles at $\xi \to \pm\infty$ that corresponds to the limit $t \to t_0$. In this limit, for $x - x_0 \neq 0$ (away from the singularity location), the singular solution must match the time independent outer solution [27]. Hence, the boundary conditions for the above ODE system is obtained by setting the time derivative terms on the left hand sides of Eq. (17) to zero:

$$\big(\xi\, R\big)' = 0, \;\; \big(\xi\, \Phi\big)' = 0, \;\; \xi\, E' = 0, \qquad \xi \to \pm\infty \tag{19}$$

implying

$$R \propto \xi^{-1}, \;\; \Phi \propto \xi^{-1}, \;\; E \propto \xi^{-a}, \qquad \xi \to \pm\infty \tag{20}$$

for any choice of $a \geq 1$. The precise similarity profiles R, Φ and E can in principle be obtained by solving the nonlinear ODE system Eq. (17), subject to boundary conditions Eq. (18) and Eq. (20). Note that, as the singularity is approached at $t \to t_0$, the strain dependent turnover term, $e^{\alpha\epsilon} \sim e^{\alpha \ln(t_0-t) E(\xi)} \to 0$. This provides an aposteriori justification for our neglect of turnover in our scaling analysis.

Numerical solutions of the blowup. We use Dedalus pseudospectral solver [35] to solve the system of PDEs Eqs. (1) in 1D, with variables represented on a periodic Fourier basis. Periodic basis functions like the Fourier basis provide exponentially converging approximations to smooth functions. The fast Fourier transform (implemented using sciPy and FFTW libraries [35]) enables computations requiring both the series coefficients and grid values to be performed efficiently. For time evolving the system of equations, we use a SBDF2 timestepper, a 2nd-order semi-implicit Backward Differentiation formula scheme [36]. Our initial conditions are a homogeneous unstrained symmetric mixture $\phi = 0$, to which we add noise sampled from a uniform distribution between $[-0.1, 0.1]$. We use 500 modes ($N = 500$) in a domain length of $L = 35$ and a time-step (dt) of 10^{-4} to solve Eqs. (1). We use the following set of parameters:

$B = 10$, $C = 1$, $D = 1$, $k_1 = 1$, $k_2 = 0$, $k^b_{\rm rel} = 0$, $k_3 = 1$, $\zeta_{\rm avg} = 3$, $\zeta_{\rm rel} = 2$, $k_4 = 2$, $\chi(\rho^0_a) = 1$, $\chi'(\rho^0_a) = 0.01$, $\chi''(\rho^0_a) = 0.001$, $\chi'''(\rho^0_a) = -0.001$.

On solving we find that after the initial linear stability regime, singularities in ρ, ϕ and ϵ develop in regions of high myosin density. The profiles of ϕ and ϵ near the singularity, at different time points, are shown in Fig. 4(a) and Fig. 4(c), respectively. We numerically determine the first blowup time t_0 and location x_0, from the divergence of the maximum (minimum) value of ϕ (ϵ), as seen in the insets of Fig. 4(a), (c). In agreement with our scaling analysis, we see an excellent collapse of the data for the scaled profiles of ϕ and ϵ, see Figs. 4(b), (d). This agreement between the numerical solutions of Eqs. (1) and the scaling analysis of Eqs. (11) reaffirms the irrelevance of myosin turnover in the neighbourhood of the singularity.

Since our numerical method, does not allow us to approach the singular point arbitrarily closely, we use our numerics to test the asymptotic convergence of the profiles approaching the singularity. We employ the Cauchy-convergence criterion for the sequence $\phi(x, t_n)$, for a fixed value of x near x_0 and where the sequence $\{t_n\}$ steadily approaches t_0. In Fig. D10, we have plotted $\phi(x, t_{n+1}) - \phi(x, t_n)$ as a function of t_n, at three spatial locations $x - x_0 = 0$, $x - x_0 = 0.6$, and $x - x_0 = 1$. We see that $\phi(x, t_{n+1}) - \phi(x, t_n) \to 0$ faster for points closer to the centre of the profile; the convergence rate is maximum at ϕ_{max}.

These singularities are *physical* in that their resolution involves incorporation of additional physical effects such as steric hindrance (represented by the ϵ^4 term in w). With this, the singularity is never reached, resulting in highly concentrated tensile regions of finite width, which could be taken to be the size of non-muscle myosin-II bipolar filaments [12].

The appearance of finite time elastic singularities that lead to zones of high concentration of both the actin meshwork and myosin stresslets is reminiscent of caustics discussed in the context of the Zel'dovich model for the formation of large scale self-gravitating structures of the universe [37] and verified in extensive numerical simulations, such as in [38]. We observe that at the blowup location $x = x_0$ where $\epsilon \approx -1$ (Fig. 3(c)), actin meshwork density in the deformed or Eulerian configuration $\tilde{x}_t(x) = x + u(x, t)$, given by $\tilde{\rho}_a(\tilde{x}_t(x)) = \frac{\rho_a}{1+\epsilon} = \frac{\rho^0_a - (C/A)\epsilon}{1+\epsilon}$, goes to $+\infty$ as $t \to t_0$. Moreover, this meshwork density blowup occurs before the stresslet density blowup, as seen both from the similarity forms in Eq. (16) which shows that the strain rate $\dot{\epsilon} \to -\infty$ faster than $\rho_i \to \infty$, at the same spatial blowup location x_0, and from the numerical solution (see Fig. D8). These *elastic caustics* as singularities of Lagrange maps $\tilde{x}_t \colon \mathbb{R}^d \to \mathbb{R}^d$ in higher dimensions will appear as more general Lagrangian catastrophes [37, 39], of a variety of co-dimensions (points, lines, surfaces etc.) and topology, where the associated deformation map $\partial_x \tilde{x}_t$ degenerates.

We note from our 1D numerical analysis, that the maximum strain magnitude within singular structures is of order 0.8 while outside it can reach a value of 2.5, suggesting that geometrical nonlinearities are significant. This will be particularly relevant in 2D.

V. MOVING, MERGING AND COARSENING OF SINGULARITIES

In the above scaling analysis, we have assumed that the singular structures are described by symmetric profiles of the fields, which lead to static finite-time singularities. However, our numerical analysis shows that the singular structures, tempered by steric hindrance, can move. Such *moving* singularities must be associated with an asymmetry in its density profile and discontinuities in bulk stress and mass flux across it. Indeed moving singularities show up as moving stress fibres whose interactions and coalescence have been reported in *in vivo* studies [5].

Before proceeding, we draw attention to the study of the *nucleation* instability of clusters of bound myosin [25], as opposed to the *spinodal* instability studied here. We show that on nucleating a symmetric myosin pulse of finite width, the pulse grows if the amplitude is beyond a threshold, else it relaxes to a uniform background. Further, on nucleating an asymmetric pulse, a large enough asymmetry drives a translational instability. Using a boundary layer analysis, we derive analytical forms for the asymmetric myosin density and strain profile and its velocity [25]. This information will be useful in the analysis presented below.

Isolated moving singularity. The moving singularity at $x_0(t)$ carries with it the singular component of all the bulk fields, accompanied by jumps across $x_0(t)$. We denote the jump of the limiting values (i.e., difference between right and left) of bulk fields at $x_0(t)$ by $[\![\,]\!]$ and their average by $\langle\rangle$. Continuity of the bulk displacement field u (i.e., $[\![u]\!]$=0) implies the velocity compatibility condition [40], a kinematic requirement:

$$[\![\dot{u}]\!] + V\,[\![\epsilon]\!] = 0, \tag{21}$$

where $V := \dot{x}_0$ denotes material velocity of the singular point. The spatial velocity of the singularity is then defined by $v_S := \langle \dot{u} \rangle + V \langle \epsilon \rangle$. The force and mass balance equations at the singularity can be obtained, using the divergence theorems for discontinuous fields, as

$$\Gamma_S v_S = [\![\sigma]\!], \tag{22a}$$

$$\dot{\rho}_S - V[\![\rho]\!] = -[\![j]\!] + \Pi_S, \tag{22b}$$

where Γ_S is the friction coefficient at the singularity, ρ_S is the stresslet density at the singularity, $j := -D\partial_x\rho + \rho\dot{u}$ is the bulk mass flux and Π_S is the (strain dependent) singular turnover term (see [41] for derivation in 2D).

Interacting moving singularities. When the number density of singularities is high, they will interact with each other via the long-range elastic strain. Since the moving singularities are associated with an asymmetric density profile, there could be additional non-reciprocal

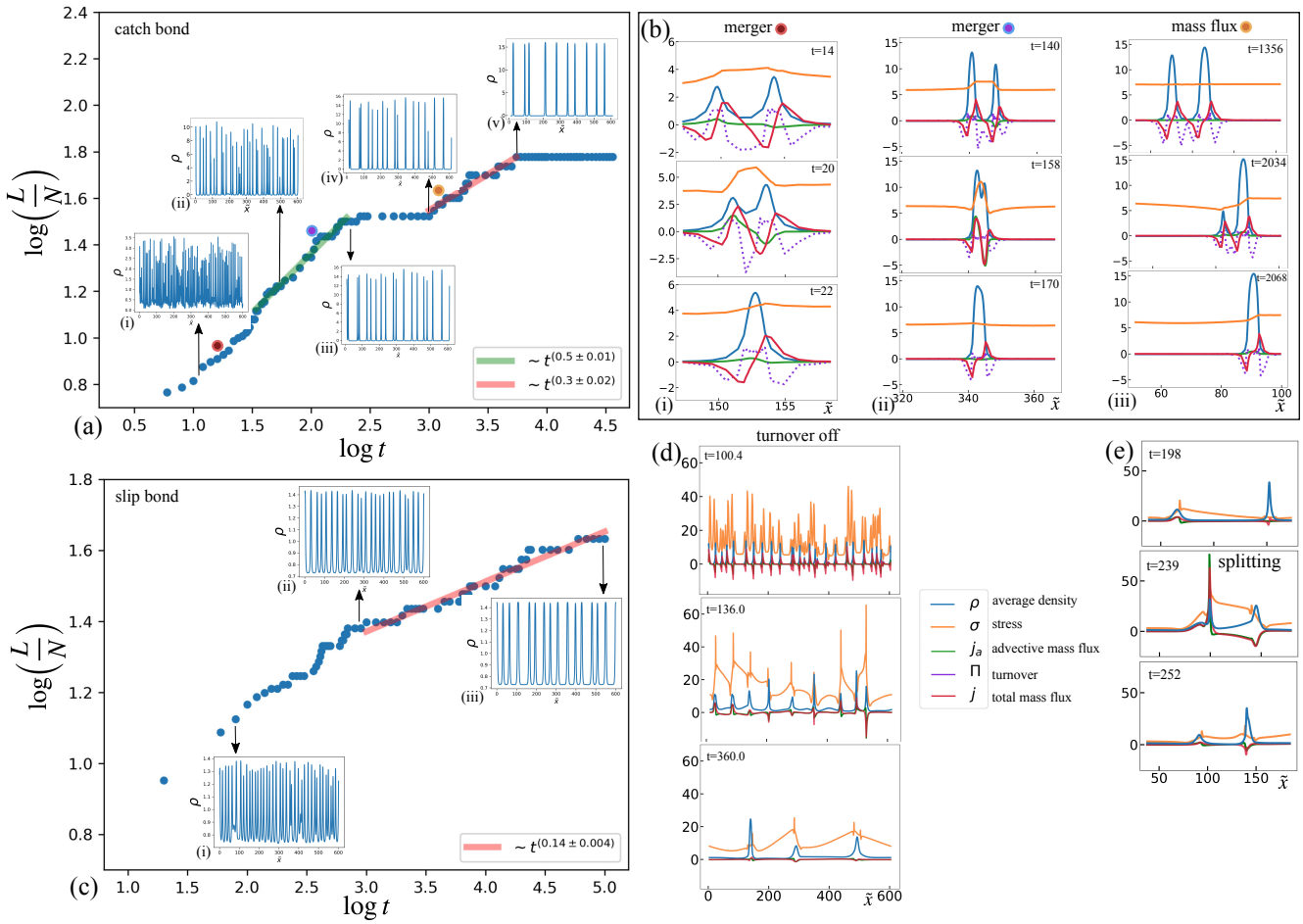

FIG. 5. **Merging of singular structures and coarsening dynamics.** In figure (a) we see coarsening dynamics for a system with catch bond. The system of equations are numerically solved for the following set of parameters : $B = 5, \chi(\rho_a^0) = 1, \chi(\rho_a^0)' = 1, \chi(\rho_a^0)'' = 0.1, \chi(\rho_a^0)''' = 15, \zeta_{avg} = 1.4, \zeta_{rel} = 1$, $k_4 = 1$, $k_3 = 2$. Panel (b) describes the dynamics of merger events driven by stress gradients and mass flux via snapshots from the numerical simulation described in (a). Panel (c) captures the coarsening dynamics for a system with slip bond. All the parameters remain unchanged apart from $k_3 = -0.5$. Panel (d) shows how the configurations generated in the numerical simulation in (a) at $t = 100$, evolve after the turnover is switched off. The jump in total flux $[\![j]\!]$ and stress $[\![\sigma]\!]$ is much higher in the absence of turnover and the merger events proceed faster as seen from the snapshots. (e) Sequence of snapshots showing splitting of singular structures after the turnover is switched off (see Movie 5).

interactions between them, possibly leading to dynamical phenomena discussed in [42, 43].

Merging and Coarsening. Thus far we have established that following the initial segregation and finite time collapse, we are generically left with a distribution of moving and interacting singularities. Subsequent evolution involves the merger and subsequent coarsening of singularities. There are two important features of this coarsening dynamics that emerge from our 1D analysis – (i) because of the long range strain, and velocity compatibility Eq. (21), the analysis of the dynamics of merger needs to be global, and (ii) coarsening proceeds so as to make the stress homogeneous, i.e. $\sigma = const.$, except at isolated points associated with the singularities. This is reflected in the time dependence of $\int (\partial_x \sigma)^2 \, dx$ (see Fig. D9), which shows an overall decrease in time, except at isolated time points associated with the onset of singularity mergers, a kind of Lyapunov functional.

We see that the inverse density of singularities L/N which measures the typical distance between singularities, grows initially and then saturates, see Fig. 5(a) and (c), for the cases where both the species are of catch and slip type, respectively. The power law growth associated with early time coarsening is indicated in the figures. The saturation at late times, either indicate arrested coarsening or at most a slow logarithmic growth indicative of activated dynamics.

To understand the dynamics of coarsening, we monitor the time dependence of the local fields, stresses and currents. Soon after the establishment of the distribution of

singularities, the number density of singular structures is high and the variation in the heights of the singular density profiles ρ_{S_i} is large (Fig. 5(a), inset (i), and Movie 4). As a result all the driving jump terms $[\![\rho]\!]_i$, $[\![j]\!]_i$ and $[\![\sigma]\!]_i$, across each singularity i, are large, leading to a large speed V_i and large mass flux $\dot{\rho}_{S_i}$ out of/into the singularities (Fig. 5(b)(i)). This drives merger, since the elastic energy barrier between neighbouring singularities are easily overcome, and results in fast coarsening with a rate $t^{0.5}$ (Fig. 5(a), green line). After several merger events, the singularities get sparser, the variation in the heights of the singularities gets smaller (Fig. 5(a), insets (ii,iii,iv)), the jumps in the fields and the mass flux across the singularities become smaller – and as a result, the elastic stress gets more homogeneous (Fig. 5(b)(ii)). Together, this leads to a slower coarsening with a rate $t^{0.3}$ (Fig. 5(a), pink line), associated with a driving force that mainly comes from the advective current flowing from slightly smaller singularities to higher ones, (and to a lesser extent through the turnover of myosin), see Fig. 5(b)(iii). We note that the fitted growth exponents reported here represent intermediate time dynamics, and are not universal. For $k_3 < 0$, i.e., slip bond response, the coarsening gets much slower with a rate $t^{0.14}$ (Fig. 5(c) and Movie 6).

Eventually the variation in the heights of the singularity profiles vanishes, and the dynamics reaches a steady state, thus, arresting the coarsening, with a distinct distribution of singular structures, see the plateau in Fig. 5(a) and inset (v).

Interestingly, we find that myosin turnover, is crucial in maintaining this dynamics of singular structures. If we switch off the turnover during this coarsening stage, say at $t = 100$ in Fig. 5(a), we find a large increase in the mass flux from diffusion and advection, causing the singular structures to spread and overlap, leading to merger and faster coarsening, see Fig. 5(d) and Movie 5. Splitting of singularities is also observed, see Fig. 5(e) and Movie 5, that is reminiscent of stress fiber splitting reported in [5, 44]. Eventually this will result in a single domain with high myosin density, a contractile collapse, as predicted by the phase diagram when the turnover rates are set to zero. In vivo, this eventuality can be interrupted by anchoring on other extended structures such as microtubules or membranes.

Thus, material renewability provides a control of the coarsening dynamics, maintaining the distribution and organisation of the singular force structures.

VI. ACTIVE RENEWABILITY DRIVES EXCITABILITY

Apart from the contractile and segregation instabilities, the linear stability analysis of the hydrodynamic equations Eq. (1) also predicts a variety of oscillatory phases. As before, this is decided by the behaviour of the λ_{max}, the largest eigenvalue (Eq. (7)) of the dynamical matrix $\mathbf{M}$.

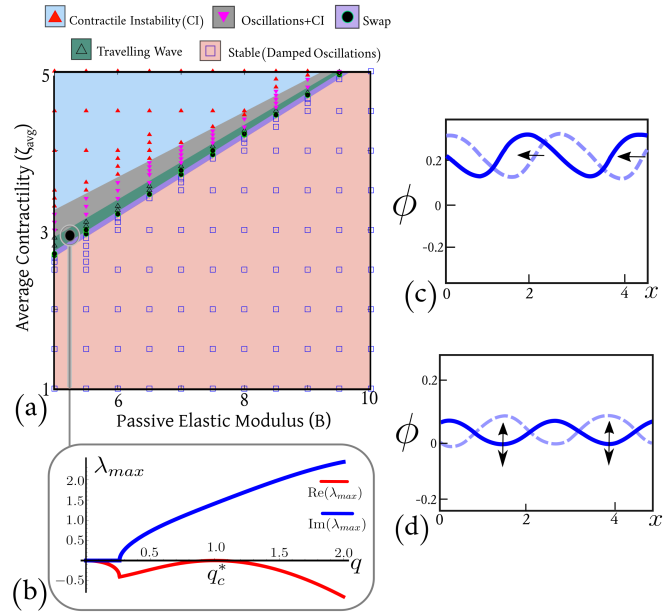

FIG. 6. **Numerical phase diagram and nature of oscillatory phases.** (a) Full phase diagram obtained by numerically solving the scalar version of (1), for $\zeta_{\rm rel}k_4 < 0$, showing successive emergence of swap and travelling waves from the stable phase (with damped oscillations) with increasing average contractility. Symbols denote the state points where the numerical solutions were obtained. Details of numerical solutions are described in the text. (b) Typical dispersion curve obtained from linear stability analysis for the travelling wave phase, where the mode $q_c^\star$ is the fastest growing mode that first reaches criticality. (c,d) Snapshots of ϕ-profiles (blue line) and their time-evolution (dashed line with progressively dark hues of blue accompanied by arrows) showing (c) travelling wave (Movie 7) moving to the left and (d) standing wave (swap) behaviour (see Movie 8).

From the form of λ_{max}, we see that $\lambda_b < 0$ characterizes the various oscillatory phases (stable and unstable pulsations and/or waves), with frequency $\omega(q) = |\,\mathrm{Im}(\lambda_{max})|$, and decay/growth rate $\tau_d(q) = |\,\mathrm{Re}(\lambda_{max})|$. The oscillations are stable (damped oscillations) for $Re[\lambda_{max}] < 0$, i.e., when $\lambda_a > 0$, and unstable (growing oscillations) for $Re[\lambda_{max}] > 0$, i.e., when $\lambda_a < 0$. Unstable oscillations grow with a fastest growing mode at a wave vector $q^\star$. The fastest growing mode $q = q^\star$, characterized by $\partial_q Re[\lambda_{max}](q^\star) = 0$, is

$$q^\star = \sqrt{-1 + \sqrt{\frac{-(\tilde{B} + \mu) + \frac{2\zeta_{\rm avg}}{k_1}}{D}}}. \tag{23}$$

At the transition from stability to instability, the fastest growing mode becomes critical: $\lambda_a(q^\star) = 0$, yielding

$$\left(\sqrt{-(\tilde{B} + \mu) + \frac{2\zeta_{\rm avg}}{k_1}} - \sqrt{D}\right)^2 = k_1, \tag{24}$$

as a mode independent characterization of marginal stability/criticality in the oscillatory phase. Using this relation in (23), we find the critical wave vector for travelling waves is $q_c^\star = \sqrt[4]{\frac{k_1}{D}}$. At $q = q_c^\star$, the frequency is given by (recall that $\lambda_a(q_c^\star) = 0$)

$$\omega(q_c^\star) = \frac{\sqrt{\frac{k_1}{D}}}{\sqrt{1+\sqrt{\frac{k_1}{D}}}}\Bigg((\tilde{B}+\mu)\sqrt{Dk_1} + k_1\Bigg((\tilde{B}+\mu) - 2\frac{\zeta_{\rm avg}}{k_1}\left(\frac{C}{A}+\frac{k_3}{k_1}\right) - 2\frac{\zeta_{\rm rel}}{k_1}\frac{k_4}{k_1}\Bigg)\Bigg)^{\frac{1}{2}}. \tag{25}$$

Hence, for fixed values of

$$\tilde{B}+\mu > 0 \;\text{ and }\; \tilde{B}+\mu - 2\frac{\zeta_{\rm avg}}{k_1}\left(\frac{C}{A}+\frac{k_3}{k_1}\right) > 0\,,$$

we must have $\zeta_{\rm rel}k_4 < 0$ for $\omega(q_c^\star)$ to be real, i.e, $\zeta_{\rm rel}$ and k_4 should be of opposite signs. If $\zeta_{\rm avg} > \zeta_{\rm rel}$, then one should have $\alpha_1 < \alpha_2$ to trigger the travelling wave phase. Since the stresslets are contractile, i.e., $\epsilon < 0$, this implies that $k_1^u(\epsilon) > k_2^u(\epsilon)$. Hence, in order to have travelling waves, the species with larger activity must unbind more than the species with lower activity.

In addition to the travelling wave there is another oscillatory phase called the Swap phase [29], charaterized by standing wave solutions of the form $\phi(x,t) = \sin(qx)\sin(\omega t)$. This cannot be obtained directly from the behaviour of the dispersion curves as above. Instead we argue as follows: in the linear regime, the onset of the contractile instability is dictated by the time scale $Re[\lambda_{max}(q)]^{-1}$, while the time scale of unbinding of the stronger stresslet (i.e., ρ_1) is $k_1^u(\epsilon)^{-1}$. Within the oscillatory phase, i.e., when $\zeta_{\rm rel}k_4 < 0$, if the stronger stresslet unbinds before the contractile instability kicks in, i.e., if

$$Re[\lambda_{max}(q)]^{-1} \leq k_1^u(\epsilon)^{-1}, \tag{26}$$

then the contracting domain expands again before ever reaching the contractile instability. This swap phase occurs at the boundary between the damped wave phase and mechanical instability phase.

The complete phase diagrams, obtained from numerically integrating the PDEs Eq. (1), are qualitatively similar to the linear stability phase diagrams, apart from the appearance of sustained oscillatory phases such as travelling waves and swap. At the boundary between the oscillatory phases and the contractile instability, we see a travelling wave train with amplitude that grows indefinitely, giving rise to an array of moving tension lines. Similarly, the swap phase occurs at the boundary between the damped wave phase and mechanical instability phase. In addition, in a regime of parameter space, the numerical phase diagram displays phases with very long transients followed by an eventual settling down into a phase which is very different from the one predicted by the linear stability analysis (Movie 9, Movie 10).

This breakdown of modal analysis [45, 46], is because the dynamical matrix $\mathbf{M}$ describing linear instabilities to imposed perturbations, is non-Hermitian due to TRS breaking. As a consequence, the three eigenvectors along which the perturbations propagate are no longer orthogonal to each other and co-align in four different ways for some parameter values. Such points are called *exceptional points* (dashed line in Fig. 2) – as we move through parameter space, hypersurfaces of different types of exceptional points [29, 30] separate the monotonic segregation instability discussed so far from the oscillatory instabilities via Hopf bifurcations. In such cases, even though linear stability predicts (for a particular parameter regime) the existence of a monotonically stable phase, numerical analysis of the linearised equations show the existence of growing oscillations.

Indeed, conclusions about various phases drawn from the above linear stability analysis are robust only in regions far from the Exceptional Points (EPs) of the non-Hermitian dynamical matrix $\mathbf{M}$, where eigenvalues coalesce and eigenvectors co-align. Near EPs, the system undergoes strong transient growth and 'bootstraps' into nonlinear phases. We will analyse the effect of EPs in the mechanics of active matter in a later publication. We only mention here that in the above linear stability phase diagrams, the only EPs present are on the boundary between monotonically stable and damped wave phases. Hence, the system goes into the oscillatory phase through an EP.

For $\zeta_{\rm rel}k_4 < 0$, we observe from numerical phase diagram Fig. 6(a) that there is a region where travelling waves and swap are *coexisting phases in time*. That is, starting with random perturbations about the uniform, symmetric unstrained steady state in the parameter regime $\zeta_{\rm rel}k_4 < 0$, sustained oscillations appear at the unstable wave and stable wave phase boundary, either as a travelling wave train, or as a standing wave (i.e., swap). Typically the system exhibits a long transient, where it first goes into a swap phase, then a coexistence between swap and travelling wave, and then finally transitions into a travelling wave. The transient time decreases with an increase in the average contractility. The numerical phase diagram (Fig. 6) is constructed from the configurations obtained at an arbitrarily chosen large time, $t_{max} = 1000$.

The full phenomenology of such temporally coexisting nonequilibrium phases is very complex and we leave a detailed exposition for later.

VII. DISCUSSION

Renewable active matter is a new kind of active matter with novel mechanical properties displaying elastic marginality, force chains, mechanical fragility and spontaneous excitability [4, 18, 25, 41]. In this paper we have studied how the interplay between activity and material renewability can give rise to unusual segregation and

nonequilibrium force patterning in living materials. A striking example is the cell spanning active cytoskeleton, where a variety of myosin species act as molecular force generators and sensors to give rise to striking singular extended structures carrying tension (e.g., stress fibres).

Here we derive hydrodynamic equations in terms of the local strain and the densities of two types of myosin species that differ in their contractility and turnover rates, but which otherwise do not interact with each other. Despite this, the two myosin species undergo a spinodal segregation instability, with myosin density patterns that depend on the nature of the strain-dependent unbinding, namely, whether they have catch or slip bond response.

Subsequently the spinodal patterns become unstable due to a nonlinear coupling between the linear segregation and contractile instability. This drives domain shrinkage, leading to a finite-time singularity where the density and elastic fields display scaling behaviour. We formally associate the distribution of these singular structures with caustics. These singular structures or caustics move, merge and coarsen over time. The rate of coarsening gets slower as time progresses and eventually gets arrested. This segregation of myosin species into singular structures immediately implies spatiotemporal force patterning that spans across the system. Importantly, *material renewability in the form of myosin turnover, is crucial in maintaining this dynamics and eventual arrest of singular structures, and thus force patterning.* In the cellular context, one needs to include active boundary conditions at the cell surface in the form of focal adhesions and adherent junctions, whose strength and positioning will select specific bulk force patterns. In addition, force patterning within the cell are affected by other spatially extended structures, such as microtubules and internal membranes.

From an evolutionary materials perspective, our work suggests that by evolving neutrally in the space of myosin binding/unbinding affinities and contractility, can give rise to favourable phenotypes, such as, differences in cellular localisation and the patterning of a network of forces across the scale of the cell. Further, in the context of *physical learning* [47], our work provides insights on active materials synthesis whose components learn parameter values that drive it towards specific material response, such as mechanical adaptation [48] and tensegrity [49].

In addition, the system exhibits a variety of oscillatory force patterns such as travelling waves, swap, and their temporal coexistence, that are accessed through exceptional points of the underlying non-reciprocal dynamics. The 3-dimensional non-Hermitian dynamical matrix describing the instabilities to linear perturbations, leads to different kinds of exceptional manifolds. This and the exploration of the coexisting temporal phases using nonmodal analysis, will be taken up in a later study.

We will, in another publication, extend our analysis to a fully tensorial elasticity in two dimensions; while this extension is nontrivial, the basic message of segregation followed by a finite time collapse survives. This will allow us to make direct comparisons to the dynamical patterning of stress fibres, such as those observed in experiments in cells [50] and in cell extracts on micropatterned substrates [5, 51, 52].

VIII. ACKNOWLEDGEMENTS

We thank members of the Simons Centre at NCBS for clarifying discussions. We acknowledge support from the Department of Atomic Energy (India) under project no. RTI4006, the Simons Foundation (Grant No. 287975) and the computational facilities at NCBS. MR acknowledges Department of Science and Technology (India), for a JC Bose Fellowship (SERB File No.JCB/2018/00030).

Appendix A: Hydrodynamic Equations for a Mixture of Contractile Stresslets on an Elastomer

We describe the dynamics of active stress propagation in the active medium of the cell using hydrodynamic equations for the crosslinked actin mesh and the density of different species of myosin filaments, embedded in the viscous cytosol.

A1. Equations for the Crosslinked Actin Meshwork embedded in the Cytosol

We start with a passive d-dimensional elastomeric meshwork of mass density ρ_a, whose displacement with respect to an unstrained reference state is $\boldsymbol{u}$. The meshwork moves in the fluidic cytosol whose velocity is $\boldsymbol{v}$. The hydrodynamic equations for its linear momentum balance and mass balance are, therefore,

$$\rho_a \ddot{\boldsymbol{u}} + \Gamma\left(\dot{\boldsymbol{u}} - \boldsymbol{v}\right) = \nabla \cdot \boldsymbol{\sigma}, \quad \text{and} \tag{A1a}$$

$$\dot{\rho_a} + \nabla \cdot \left(\rho_a \, \dot{\boldsymbol{u}}\right) = M \nabla^2 \frac{\delta F}{\delta \rho_a} + \mathcal{S}_a. \tag{A1b}$$

Here, $\Gamma > 0$ is the friction coefficient of the elastomer with respect to the fluidic cytosol, and $\boldsymbol{\sigma}$ is the total stress in the elastomer; M represents the mobility of permeation of the meshwork, and $\mathcal{S}_a$ represents turnover of the actin meshwork. F is the free energy functional for the passive meshwork:

$$F(\boldsymbol{\epsilon}, \rho_a) = \int_\Omega f_B \, d^d r; \tag{A2}$$

where the free energy density $f_B(\boldsymbol{\epsilon}, \rho_a)$ depends on the linearized strain $\boldsymbol{\epsilon} := (\nabla \boldsymbol{u} + \nabla \boldsymbol{u}^T)/2$ of the elastomer, and the mass density ρ_a.

The hydrodynamic equations of the fluidic cytosol are given by

$$\rho_f\Big(\dot{\boldsymbol{v}}+\boldsymbol{v}\cdot\nabla\boldsymbol{v}\Big) = \eta_f^s\nabla^2\boldsymbol{v}+\Big(\eta_f^b+\frac{\eta_f^s}{d}\Big)\nabla(\nabla\cdot\boldsymbol{v})-\nabla p+\Gamma\,(\dot{\boldsymbol{u}}-\boldsymbol{v}); \tag{A3}$$

here, ρ_f is the density of the fluid, and η_f^s and η_f^b are the shear and bulk viscosities of the fluid. The fluid pressure p appears due to the total incompressibility of the meshwork-fluid system:

$$\nabla\cdot\Big(c_a\,\dot{\boldsymbol{u}}+(1-c_a)\boldsymbol{v}\Big) = 0; \tag{A4}$$

here, c_a is volume fraction of the meshwork. Here, for convenience, we ignore the hydrodynamics of the fluid, permissible in the limit when $c_a \approx 1$.

A2. Equations for the Stresslets

Consider a mixture of active contractile stresslets with different contractilities undergoing turnover onto this elastomer. We assume that the stresslets binding onto the elastomer are recruited from an infinite pool of stresslets unbound to the elastomer, and, hence, disregard the dynamics of these unbound stresslets. Restricting to a binary mixture, let ρ_i, $i = 1, 2$, be the density fields of the two species of bound stresslets. The bound stresslets get advected by the local velocity $\dot{\boldsymbol{u}}$ of the elastomer, and diffuse on it with the same diffusion coefficient D. Let the stresslets bind onto the elastomer with rates $k_i^b > 0$, and unbind from the elastomer with rates $k_i^u(\boldsymbol{\epsilon}) > 0$ that in principle depends on the strain $\boldsymbol{\epsilon}$ of the elastomer. The dynamics of these bound stresslets is, hence, governed by

$$\dot{\rho}_i + \nabla\cdot(\rho_i\,\dot{\boldsymbol{u}}) = \nabla\cdot(D\,\nabla\rho_i) + k_i^b\,\rho_a - k_i^u(\boldsymbol{\epsilon})\,\rho_i. \tag{A5}$$

We will assume the Hill form for the unbinding rates: $k_i^u(\boldsymbol{\epsilon}) = k_{i0}^u\,e^{\alpha_i\,\epsilon}$, $i = 1, 2$ where $k_{i0}^u > 0$, $i = 1, 2$, are the strain independent parts of the respective rates, $\epsilon := \mathrm{tr}\,\boldsymbol{\epsilon}$ is the dilational strain, and the dimensionless numbers α_i capture whether the bond is catch or slip type: $\alpha_i > 0$ ensures that local contraction (extension) will decrease (increase) the unbinding of the stresslets, i.e., the bond is of catch type, while $\alpha_i < 0$ ensures that local contraction (extension) will increase (decrease) the unbinding of the stresslets, i.e., the bond is of slip type.

In the small timescale of the turnover processes of the stresslets comparatively larger than the turnover of the crosslinked actin meshwork, the elastomer can be considered as long lived, i.e., right hand side of (A1b) is zero. This implies that elastomer density ρ_a is enslaved to the isotropic strain of the elastomer: $\delta\rho_a \propto -\epsilon$ (obtained from a variation of (A6) below); here, $\delta\rho_a := \rho_a - \rho_a^0$ is the deviation of the elastomer density from its state value ρ_a^0

A3. Constitutive Equations

The elastic stress $\boldsymbol{\sigma}^e := \frac{\delta F}{\delta\boldsymbol{\epsilon}}$ comes from the free-energy functional $F(\boldsymbol{\epsilon},\rho_a) = \int d^2r f_B$ of an isotropic linear elastic medium, where

$$f_B = \frac{1}{2}B\epsilon^2 + \mu|\tilde{\boldsymbol{\epsilon}}|^2 + C\,\delta\rho_a\,\epsilon + \frac{A}{2}\delta\rho_a^2 + \frac{K}{2}|\nabla\epsilon|^2 \tag{A6}$$

is the free energy density; with the elastic moduli B, $\mu > 0$, and $C > 0$, $A > 0$ from thermodynamic stability. The isotropic elastic stress is

$$\begin{aligned}\boldsymbol{\sigma}^e = \frac{\delta F}{\delta\boldsymbol{\epsilon}} &= \Big(B\,\epsilon + C\,\delta\rho_a - K\nabla^2\epsilon\Big)\,\mathbf{I} + 2\mu\tilde{\boldsymbol{\epsilon}} \\ &= \Big(B - \frac{C^2}{A}\Big)\,\epsilon\,\mathbf{I} - K\nabla^2\epsilon\,\mathbf{I} + 2\mu\tilde{\boldsymbol{\epsilon}},\end{aligned} \tag{A7}$$

noting that $\delta\rho_a = -\frac{C}{A}\epsilon$. The elastic modulus B of the actin mesh is set by the crosslinker density. The passive viscous stress of the elastomer is $\boldsymbol{\sigma}^d = \eta_b\,\dot{\epsilon}\,\mathbf{I}+2\eta_s\,\dot{\tilde{\boldsymbol{\epsilon}}}$, where $\eta_{b,s}$ are the bulk and shear viscosities, respectively.

At the macroscopic/coarse-grained scale, the isotropic active stress $\boldsymbol{\sigma}^a$ is of the form $\boldsymbol{\sigma}^a = \Delta\mu\,\chi(\rho_a)\zeta(\{\rho_i\})\mathbf{I}$, where $\Delta\mu$ is the chemical potential change due to ATP hydrolysis, and $\chi(\rho_a)$ is a sigmoidal function that encodes the dependence of the active stress on the meshwork density. We will take $\Delta\mu = 1$ for simplicity.

In case of mixtures, we assume that the stresslets do not interact directly but only via the strain of the elastomer. Hence, the function $\zeta(\{\rho_i\})$ can be additively decomposed into individual contributions coming from each stresslet species, i.e., $\zeta(\{\rho_i\}) = \sum_i \zeta_i(\rho_i)$. We assume the functions $\zeta_i(\rho_i)$ to be linear in ρ_i, i.e., $\zeta_i(\rho_i) = \zeta_i\rho_i$ (no sum over i) where the contractilities $\zeta_i > 0$ are different for different species i. For a binary mixture, Taylor expanding the function $\chi(\rho_a)$ about the state value $\rho_a = \rho_a^0$ upto cubic order leads to

$$\begin{aligned}\boldsymbol{\sigma}^a &= \chi(\rho_a)\Big(\zeta_1\,\rho_1 + \zeta_2\,\rho_2\Big)\mathbf{I} \\ &= \left(\chi(\rho_a^0) - \chi'(\rho_a^0)\frac{C}{A}\,\epsilon + \frac{1}{2!}\chi''(\rho_a^0)\left(\frac{C}{A}\,\epsilon\right)^2 - \frac{1}{3!}\chi''(\rho_a^0)\left(\frac{C}{A}\,\epsilon\right)^3 + O(\epsilon^4)\right)\times 2\Big(\zeta_{\rm avg}\,\rho + \zeta_{\rm rel}\,\phi\Big)\mathbf{I},\end{aligned} \tag{A8}$$

where we have introduced the the average and the relative densities of the bound stresslets:

$$\rho := \frac{\rho_1+\rho_2}{2} \quad\text{and}\quad \phi := \frac{\rho_1-\rho_2}{2}; \tag{A9}$$

and

$$\zeta_{\rm avg} := \frac{\zeta_{\rm avg}+\zeta_{\rm rel}}{2} > 0,\ \zeta_{\rm rel} := \frac{\zeta_{\rm avg}-\zeta_{\rm rel}}{2} \tag{A10}$$

as the average and relative contractility, respectively. Note that ϕ is the order parameter for segregation.

A4. Non-dimensional Governing Equations

We will further assume the overdamped limit of the elastomer, i.e., $|\rho_a\,\ddot{\boldsymbol{u}}| \ll |\Gamma\,\dot{\boldsymbol{u}}|$, and introduce

$$k^u_{\rm avg} := \frac{k^u_1+k^u_2}{2},\quad k^u_{\rm rel} := \frac{k^u_1-k^u_2}{2}, \tag{A11}$$

the average and relative unbinding rates, respectively;

$$k^b_{\rm avg} := \frac{k^b_1+k^b_2}{2} > 0 \ \text{ and } \ k^b_{\rm rel} := \frac{k^b_1-k^b_2}{2} \tag{A12}$$

the average and relative binding rates, respectively. Taylor expanding the Hill form of unbinding, we write

$$k^u_{\rm avg}(\epsilon) = k_1 + k_3\,\epsilon + o(|\epsilon|), \tag{A13a}$$
$$k^u_{\rm rel}(\epsilon) = k_2 + k_4\,\epsilon + o(|\epsilon|); \tag{A13b}$$

where

$$k_1 := \frac{k^u_{10}+k^u_{20}}{2} > 0,\ \text{ and } \ k_2 := \frac{k^u_{10}-k^u_{20}}{2} \tag{A14}$$

are the bare (i.e., strain independent) average and relative unbinding rates, respectively, and

$$k_3 := \frac{k^u_{10}\alpha_1+k^u_{20}\alpha_2}{2},\ \text{ and } \ k_4 := \frac{k^u_{10}\alpha_1-k^u_{20}\alpha_2}{2} \tag{A15}$$

are the coefficients of the linear strain dependent parts of the relative and average unbinding rates, respectively.

Note that if $\zeta_{\rm rel}=0$, $k_2=0$ and $k_4=0$, the distinction between the two contractile species disappears and the system becomes effectively one species. Hence, these three parameters in our model cannot be made zero simultaneously.

Let the characteristic time scale be $t^\star := 1/k^b_{\rm avg}$, the characteristic length scale $l^\star := \sqrt{\eta_b/\Gamma}$, and the characteristic density ρ^0_a. We non-dimensionalize all the variables with the following redefinitions:

$$\frac{t}{t^\star}\to t,\quad \frac{x}{l^\star}\to x,\quad l^\star\partial_x\to\partial_x,\quad l^{\star 2}\partial^2_{xx}\to\partial^2_{xx} \tag{A16a}$$
$$\frac{u}{l^\star}\to u,\quad \frac{\rho}{\rho^0_a}\to\rho,\quad \frac{\phi}{\rho^0_a}\to\phi,\quad \frac{D\,t^\star}{l^{\star 2}}\to D, \tag{A16b}$$
$$t^\star\,k^b_{\rm rel}\to k^b_{\rm rel},\quad t^\star\,k^u_{\rm avg}\to k^u_{\rm avg},\quad t^\star\,k^u_{\rm rel}\to k^u_{\rm rel}, \tag{A16c}$$
$$\frac{B\,t^\star}{\Gamma l^{\star 2}}\to B,\quad \frac{C\,t^\star\rho^0_a}{\Gamma l^{\star 2}}\to C,\quad A\to A, \tag{A16d}$$
$$\frac{\zeta_{\rm avg}\,t^\star\rho^0_a}{\Gamma l^{\star 2}}\to\zeta_{\rm avg},\quad \frac{\zeta_{\rm rel}\,t^\star\rho^0_a}{\Gamma l^{\star 2}}\to\zeta_{\rm rel}. \tag{A16e}$$

With this, the non-dimensional form of the governing equations become

$$\dot{\boldsymbol{u}} = \nabla\cdot\boldsymbol{\sigma}, \tag{A17a}$$
$$\dot\rho + \nabla\cdot(\rho\,\dot{\boldsymbol{u}}) = D\,\nabla^2\rho + \left(\rho^0_a - \frac{C}{A}\epsilon\right) - k^u_{\rm avg}(\epsilon)\,\rho - k^u_{\rm rel}(\epsilon)\,\phi, \tag{A17b}$$
$$\dot\phi + \nabla\cdot(\phi\,\dot{\boldsymbol{u}}) = D\,\nabla^2\phi + k^b_{\rm rel}\left(\rho^0_a - \frac{C}{A}\epsilon\right) - k^u_{\rm avg}(\epsilon)\,\phi - k^u_{\rm rel}(\epsilon)\,\rho. \tag{A17c}$$

with

$$\boldsymbol{\sigma} = \Big(\sigma_0 + \tilde{B}\,\epsilon + B_2\,\epsilon^2 + B_3\,\epsilon^3 + \dot\epsilon - K\nabla^2\epsilon\Big)\mathbf{I} + 2\mu\tilde{\boldsymbol{\epsilon}}, \tag{A18}$$

as the non-dimensional stress, where

$$\sigma_0 := 2\,\chi(\rho^0_a)\big(\zeta_{\rm avg}\,\rho + \zeta_{\rm rel}\,\phi\big), \tag{A19}$$
$$\tilde{B} := B - \frac{C^2}{A} - 2\,\chi'(\rho^0_a)\,\frac{C}{A}\big(\zeta_{\rm avg}\,\rho + \zeta_{\rm rel}\,\phi\big), \tag{A20}$$
$$B_2 := \chi''(\rho^0_a)\left(\frac{C}{A}\right)^2\big(\zeta_{\rm avg}\,\rho + \zeta_{\rm rel}\,\phi\big), \tag{A21}$$
$$B_3 := -\frac{\chi'''(\rho^0_a)}{3}\left(\frac{C}{A}\right)^3\big(\zeta_{\rm avg}\,\rho + \zeta_{\rm rel}\,\phi\big). \tag{A22}$$

Here, σ_0 is the purely active back pressure, $\tilde{B}$ is the activity renormalized bulk modulus of linear elasticity, B_2 and B_3 are purely active nonlinear bulk moduli, which depend on ρ_1 and ρ_2. For the effective material to show contractile response, $\chi''(\rho^0_a)$ and hence B_2 needs to be positive. For stability of the nonlinear elastic material, $\chi'''(\rho^0_a)$ must be negative (rendering B_3 positive).

Appendix B: Linear Stability Analysis

B1. Homogeneous unstrained steady state

For the homogeneous unstrained steady states of the system (A17), we have $\boldsymbol{u}=\mathbf{0}$, and $\nabla\rho=\nabla\phi=\mathbf{0}$. The dynamical equations reduce to

$$k_1\,\rho + k_2\,\phi = 1, \tag{B1a}$$
$$k_2\rho + k_1\,\phi = k^b_{\rm rel}, \tag{B1b}$$

which yields

$$\rho = \rho_0 := \frac{k_1 - k_2\,k^b_{\rm rel}}{(k_1)^2-(k_2)^2},\ \text{ and } \ \phi = \phi_0 := \frac{k_1\,k^b_{\rm rel} - k_2}{(k_1)^2-(k_2)^2}. \tag{B2}$$

For $\rho_0>0$, we require either $k_1 > k_2 k^b_{\rm rel}$ and $(k_1)^2 > (k_2)^2$, or $k_1 < k_2 k^b_{\rm rel}$ and $(k_1)^2 < (k_2)^2$.

B2. Linear stability of the homogeneous unstrained steady state

To study the linearized dynamics of (A17) around the homogeneous unstrained steady state, we substitute $\boldsymbol{u} =$

$\delta\boldsymbol{u}$, $\rho = \rho_0 + \delta\rho$ and $\phi = \phi_0 + \delta\phi$ in (A17), neglect all the terms containing higher powers of $\delta\boldsymbol{u}$, $\delta\rho$ and $\delta\phi$, and obtain

$$\dot{\delta u_i} = \tilde{B}\,\delta u_{j,ji} + \mu\,\delta u_{i,jj} + 2\,\chi(\rho_a^0)\big(\,\zeta_{\rm avg}\,\delta\rho_{,i} + \zeta_{\rm rel}\,\delta\phi_{,i}\big) + \dot{\delta u}_{j,ji}, \tag{B3a}$$

$$\dot{\delta\rho} + \rho_0\,\dot{\delta u}_{i,i} = D\,\delta\rho_{,ii} - k_1\,\delta\rho - \left(\frac{C}{A} + k_3\,\rho_0 + k_4\,\phi_0\right)\delta u_{i,i} - k_2\,\delta\phi, \tag{B3b}$$

$$\dot{\delta\phi} + \phi_0\,\dot{\delta u}_{i,i} = D\,\delta\phi_{,ii} - k_1\,\delta\phi - \left(k_{\rm rel}^b\frac{C}{A} + k_3\,\phi_0 + k_4\,\rho_0\right)\delta u_{,ii} - k_2\,\delta\rho, \tag{B3c}$$

where $\tilde{B} := B - \frac{C^2}{A} - 2\chi'(\rho_a^0)\frac{C}{A}\big(\zeta_{\rm avg}\,\rho_0 + \zeta_{\rm rel}\,\phi_0\big)$ is now the (spatiotermporally constant) renormalized linear elastic modulus at the homogeneous steady state.

The Fourier transform of (B3) with respect to $\mathbf{x}$ is obtained by substituting the anstatz $\delta A(\mathbf{x},t) = \frac{1}{(2\pi)^d}\int \delta\hat{A}(t)e^{i\mathbf{q}\cdot\mathbf{x}}\,d\mathbf{q}$, where A stands for $\boldsymbol{u}$, ρ, ϕ, and $\mathbf{q}$ is the wave vector, with $q := |\mathbf{q}|$. We rewrite the resulting equations in terms of dilation mode $\hat{u}_\parallel \equiv \hat{\delta\epsilon} := \hat{\delta u}_i q_i$, the Fourier transform of $\epsilon = \operatorname{div}\boldsymbol{u}$. We do not write the dynamics of the shear mode $\hat{\delta u}_\perp := e_{ij}\hat{\delta u}_i q_j$ here as it uncouples from the rest of the dynamics (e_{ij} denotes the 2D Levi-Civita symbol, with $e_{11} = e_{22} = 0$ and $e_{12} = -e_{21} = 1$). The final linear equations (assuming the interface term $K = 0$) are

$$\dot{\hat{\delta\epsilon}} = -\frac{(\tilde{B}+\mu)\,q^2\,\hat{\delta\epsilon} + 2\,\chi(\rho_a^0)\big(\,\zeta_{\rm avg}\,\hat{\delta\rho} + \zeta_{\rm rel}\,\hat{\delta\phi}\big)q^2}{1+q^2}, \tag{B4a}$$

$$\dot{\hat{\delta\rho}} + \rho_0\,\dot{\hat{\delta\epsilon}} = -\big(D\,q^2 + k_1\big)\hat{\delta\rho} - \left(\frac{C}{A} + k_3\,\rho_0 + k_4\,\phi_0\right)\hat{\delta\epsilon} - k_2\,\hat{\delta\phi}, \tag{B4b}$$

$$\dot{\hat{\delta\phi}} + \phi_0\,\dot{\hat{\delta\epsilon}} = -\big(D\,q^2 + k_1\big)\hat{\delta\phi} - \left(k_{\rm rel}^b\frac{C}{A} + k_3\,\phi_0 + k_4\,\rho_0\right)\hat{\delta\epsilon} - k_2\,\hat{\delta\rho}. \tag{B4c}$$

We focus on the special case $\phi_0 = 0$, i.e., symmetric binary mixture. From (B2), we obtain the necessary condition to maintain this, namely, $k_{\rm rel}^b = k_2/k_1$. As a consequence we see that $\rho_0 = 1/k_1$, and $\tilde{B} = B - \frac{C^2}{A} - 2\,\chi'(\rho_a^0)\,\frac{C}{A}\,\frac{\zeta_{\rm avg}}{k_1}$. The resulting dynamical system in the Fourier space can be written as $\dot{\mathbf{w}} = \mathbf{M}\mathbf{w}$, where $\mathbf{w}(\mathbf{q},t) = \Big(\hat{\delta\epsilon}(\mathbf{q},t)\;\hat{\delta\rho}(\mathbf{q},t)\;\hat{\delta\phi}(\mathbf{q},t)\Big)^T$, and

$$\mathbf{M} = \begin{bmatrix} -\frac{(\tilde{B}+\mu)\,q^2}{1+q^2} & -\frac{2\chi(\rho_a^0)\,\zeta_{\rm avg}\,q^2}{1+q^2} & -\frac{2\chi(\rho_a^0)\,\zeta_{\rm rel}\,q^2}{1+q^2} \\ -\left(\frac{C}{A} + \frac{k_3}{k_1} - \frac{\tilde{B}\,q^2}{(1+q^2)k_1}\right) & -Dq^2 - k_1 + \frac{2\chi(\rho_a^0)\,\zeta_{\rm avg}\,q^2}{(1+q^2)k_1} & -k_2 + \frac{2\chi(\rho_a^0)\,\zeta_{\rm rel}\,q^2}{(1+q^2)k_1} \\ -\left(\frac{k_2}{k_1}\frac{C}{A} + \frac{k_4}{k_1}\right) & -k_2 & -Dq^2 - k_1 \end{bmatrix}. \tag{B5}$$

If $\lambda_i(q)$ are distinct eigenvalues of $\mathbf{M}(q)$ and $\mathbf{v}_i(q)$ are the corresponding (linearly independent) eigenvectors, then we can write the general solution as

$$\mathbf{w}(q,t) = \sum_{i=1}^{3} c_i(q)e^{\lambda_i(q)\,t}\,\mathbf{v}_i(q), \tag{B6}$$

where the coefficients $c_i(q)$ are the projections of the initial data $\mathbf{w}(q,0)$ along the respective eigenvectors: $\Big(c_1(q)\,c_2(q)\,c_3(q)\Big)^T = \mathbf{V}(q)^{-1}\mathbf{w}(q,0)$, where $\mathbf{V}(q) := \Big[\mathbf{v}_1(q)\,\mathbf{v}_2(q)\,\mathbf{v}_3(q)\Big]$ is the matrix containing the eigenvectors as columns.

The three eigenvalues, assuming $A = 1$, are $\lambda_1 = -k_1 -$

$D\,q^2$ and $\lambda_{2,3} = -\frac{\lambda_a \pm \sqrt{\lambda_b}}{2(1+q^2)}$, where

$$\lambda_a := k_1 + \left(\tilde{B} + \mu - \frac{2\chi(\rho_a^0)\zeta_{\rm avg}}{k_1} + D + k_1\right) q^2 + D\,q^4, \tag{B7a}$$

$$\lambda_b := \lambda_a^2 - 4\,q^2(1+q^2)\Bigg[(\tilde{B}+\mu)D\,q^2 + k_1\left(\tilde{B} + \mu - 2\chi(\rho_a^0)\frac{\zeta_{\rm avg}}{k_1}\left(\frac{C}{A} + \frac{k_3}{k_1}\right) - 2\chi(\rho_a^0)\frac{\zeta_{\rm rel}}{k_1}\frac{k_4}{k_1}\right)\Bigg]; \tag{B7b}$$

and the corresponding eigenvectors are

$$\mathbf{v}_1 = \begin{bmatrix} 0 \\ -\frac{\zeta_{\rm rel}}{\zeta_{\rm avg}} \\ 1 \end{bmatrix}, \quad \mathbf{v}_{2,3} = \begin{bmatrix} \frac{1}{2(1+q^2)}\frac{k_1}{k_4}\left(v_a \mp \sqrt{v_b}\right) \\ \frac{1}{2(1+q^2)}\frac{1}{k_4}\left(v_c \mp \frac{1}{k_1}\sqrt{v_b}\right) \end{bmatrix}, \tag{B8}$$

where $v_{a,b,c,d}$ have rather long expressions that we do not write here. Since the matrix $\mathbf{M}$ is non-Hermitian (due to presence of activity and turnover), its eigenvalues λ_i are not real and the eigenvectors $\mathbf{v}_i$ are not orthogonal in general. We make one further simplifying assumption: $k_2 = 0$, hence, $k^b_{\rm rel} = 0$, meaning that the bare (strain independent) part of the unbinding rates are idential (i.e., $k^u_{10} = k^u_{20}$), and the binding rates are identical as well (i.e., $k^b_1 = k^b_2$). It follows that $k_4 = \frac{k^u_{10}}{2}(\alpha_1 - \alpha_2)$.

Note that, (a) the coupling M_{12} between $\hat{\delta\epsilon}$ and $\hat{\delta\rho}$ in the $\hat{\delta\epsilon}$-equation and the coupling M_{21} between $\hat{\delta\epsilon}$ and $\hat{\delta\rho}$ in the $\hat{\delta\rho}$-equation can be of opposite signs depending upon the relative signs and magnitudes of k_3 and $\tilde{B}$; (b) the coupling M_{13} between $\hat{\delta\epsilon}$ and $\hat{\delta\phi}$ in the $\hat{\delta\epsilon}$-equation and the coupling M_{31} between $\hat{\delta\epsilon}$ and $\hat{\delta\phi}$ in the $\hat{\delta\phi}$-equation are of opposite signs when $\zeta_{\rm rel}$ and k_4 have the opposite signs; and (c) the coupling M_{23} between $\hat{\delta\rho}$ and $\hat{\delta\phi}$ in the $\hat{\delta\rho}$-equation can have any sign while the coupling M_{32} between $\hat{\delta\phi}$ and $\hat{\delta\rho}$ in the $\hat{\delta\phi}$-equation is zero. Hence, $\hat{\delta\rho}$-$\hat{\delta\phi}$ interaction is always non-reciprocal, while the $\hat{\delta\epsilon}$-$\hat{\delta\phi}$ interaction is non-reciprocal when the stronger stresslet unbinds faster; $\hat{\delta\epsilon}$-$\hat{\delta\rho}$ interaction can be non-reciprocal depending upon the relative signs and magnitudes of k_3 and $\tilde{B}$.

If $\lambda_i(q)$ are distinct eigenvalues of $\mathbf{M}(q)$ and $\mathbf{v}_i(q)$ are the corresponding (linearly independent) eigenvectors, then we can write the general solution as

$$\mathbf{w}(q,t) = \sum_{i=1}^{3} c_i(q) e^{\lambda_i(q)\,t}\,\mathbf{v}_i(q), \tag{B9}$$

where the coefficients $c_i(q)$ are the projections of the initial data $\mathbf{w}(q,0)$ along the respective eigenvectors: $\Big(c_1(q)\,c_2(q)\,c_3(q)\Big)^T = \mathbf{V}(q)^{-1}\mathbf{w}(q,0)$, where $\mathbf{V}(q) := \Big[\mathbf{v}_1(q)\,\mathbf{v}_2(q)\,\mathbf{v}_3(q)\Big]$ is the matrix containing the eigenvectors as columns.

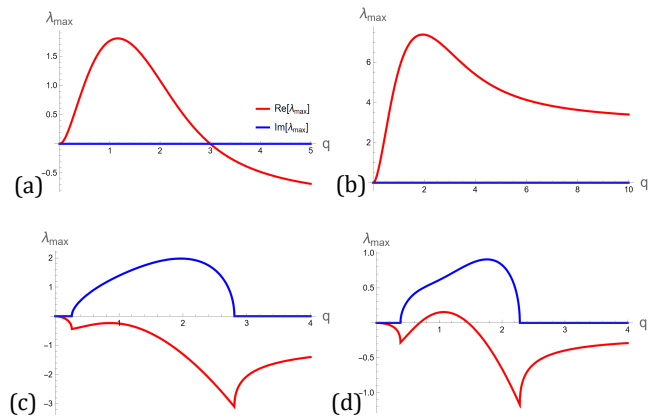

FIG. B7. Linear stability dispersion curves, with $C = 1$, $A = 1$, $D = 1$, $k_1 = 1$, $k_2 = 0$, $\chi(\rho_a^0) = 1$, $\chi'(\rho_a^0) = 1$, showing (a) segregation instability, (b) elastic contractile instability, (c) stable wave and (d) unstable wave.

Appendix C: Linear Instabilities and Phases

Our first observation is that λ_1 is real and $\lambda_1 < 0$ for all q, since $k_1 > 0$ and $D > 0$ by definition. Hence, all modes corresponding to the first eigenvalue λ_1 are asymptotically stable (i.e., monotonically decaying). Secondly, we observe that $Re[\lambda_3] \geq Re[\lambda_2]$ for all q, i.e., $\lambda_{max} = \lambda_3$. Hence, the largest eigenvalue $\lambda_{max} = \frac{-\lambda_a + \sqrt{\lambda_b}}{2(1+q^2)}$ determines the asymptotic stability of the linearized system, i.e., the 'linear' phases. We give the definitions of various phases for 1D case in Table I.

(In)stability description	*Definition*
Mechanical stability of the elastomer	$\tilde{B} + \mu > 0$
Mechanical instability of the elastomer	$\tilde{B} + \mu \leq 0$
Segregation instability	$\tilde{B} + \mu > 0,\ \lambda_b > 0,\ \lambda \geq 0$
Monotonic stability	$\tilde{B} + \mu > 0,\ \lambda_b > 0,\ \lambda < 0$
Damped oscillations	$\tilde{B} + \mu > 0,\ \lambda_b < 0,\ \lambda_a < 0$
Growing oscillations (unstable)	$\tilde{B} + \mu > 0,\ \lambda_b < 0,\ \lambda_a > 0$
Sustained oscillations (swap, travelling waves)	$\tilde{B} + \mu > 0,\ \lambda_b < 0,\ \lambda_a = 0$

TABLE I. Definition of the instabilities and phases in the linear analysis.

Based on the definitions given in Table I, we can construct various linear stability phase diagrams, which, in principle, depend on the wave vector magnitude q. The phase diagrams presented in the main text are constructed assuming q to be small, i.e., in the long wavelength limit.

C1. Segregation

When $\lambda_b > 0$, then $\lambda_{2,3}$ are real, hence, we have the monotonic stable/unstable phases. The onset of segregation instability is dictated by the sign change of λ_{max} from negative to positive.

The fastest growing mode q_{seg} is where $\partial_q \lambda_{max} = 0$. With $\chi(\rho_a^0) = \chi'(\rho_a^0) = 1$, $C = 1$, $A = 1$, $D = 1$ and $k_1 = 1$, we find

$$q_{seg} = \frac{1}{\sqrt{2}}\sqrt{\frac{B+\mu-1-2\zeta_{\rm avg}(2+k_3)-2\zeta_{\rm rel}k_4}{G}}\,, \quad \text{(C1)}$$

where

$$\begin{aligned} G := {} & B+\mu-1-6\zeta_{\rm avg}(1+k_3)+2(B+\mu)k_3\zeta_{\rm avg} \\ & -4k_3\zeta_{\rm avg}^2(2+k_3)-2\zeta_{\rm rel}k_4(3-B-\mu) \\ & -8\zeta_{\rm avg}\zeta_{\rm rel}k_4(1+k_3)-4\zeta_{\rm rel}^2k_4^2. \end{aligned} \quad \text{(C2)}$$

We observe that $\lambda_{max} = 0$ when $\lambda_a = \sqrt{\lambda_b}$, which, using (B7b), implies that

$$(\tilde{B}+\mu)\,D\,q^2+k_1\left(\tilde{B}+\mu-2\frac{\zeta_{\rm avg}}{k_1}\left(\frac{C}{A}+\frac{k_3}{k_1}\right)-2\frac{\zeta_{\rm rel}}{k_1}\frac{k_4}{k_1}\right)=0. \quad \text{(C3)}$$

The (positive) solution to this equation

$$q = \sqrt{\frac{k_1}{D(\tilde{B}+\mu)}}\sqrt{-\left(\tilde{B}+\mu-2\frac{\zeta_{\rm avg}}{k_1}\left(\frac{C}{A}+\frac{k_3}{k_1}\right)-2\frac{\zeta_{\rm rel}}{k_1}\frac{k_4}{k_1}\right)} \quad \text{(C4)}$$

is real and non-zero for $\tilde{B}_0 > 0$ if and only if

$$\tilde{B}+\mu-2\frac{\zeta_{\rm avg}}{k_1}\left(\frac{C}{A}+\frac{k_3}{k_1}\right)-2\frac{\zeta_{\rm rel}}{k_1}\frac{k_4}{k_1} < 0. \quad \text{(C5)}$$

Hence, if the condition (C5) is met, λ_3 becomes non-negative in the long wavelength limit, thus, triggering segregation instability. The characteristic width of the segregated regime is $\sim \frac{1}{q_{seg}}$.

Appendix D: Nonlinear Analysis of governing equations

These scaling forms imply the following for the derivatives,

$$\dot{\rho} = \frac{C_0}{(t_0-t)^{1+s}}\Big[s\,R(\xi)+r\,\xi\,R'(\xi)\Big], \quad \text{(D1a)}$$

$$\dot{\phi} = \frac{A_0}{(t_0-t)^{1+p}}\Big[p\,\Phi(\xi)+r\,\xi\,\Phi'(\xi)\Big], \quad \text{(D1b)}$$

$$\dot{\epsilon} = \frac{B_0}{(t_0-t)^{1+q}}\Big[q\,E(\xi)+r\,\xi\,E'(\xi)\Big], \quad \text{(D1c)}$$

and

$$\partial_x\rho = \frac{C_0}{(t_0-t)^{s+r}}R'(\xi), \quad \partial^2_{xx}\rho = \frac{C_0}{(t_0-t)^{s+2r}}R''(\xi), \quad \text{(D2a)}$$

$$\partial_x\phi = \frac{A_0}{(t_0-t)^{p+r}}\Phi'(\xi), \quad \partial^2_{xx}\phi = \frac{A_0}{(t_0-t)^{p+2r}}\Phi''(\xi), \quad \text{(D2b)}$$

$$\partial_x\epsilon = \frac{B_0}{(t_0-t)^{q+r}}E'(\xi), \quad \partial^2_{xx}\epsilon = \frac{B_0}{(t_0-t)^{q+2r}}E''(\xi), \quad \text{(D2c)}$$

where, $(\cdot)'$ denotes differentiation with respect to ξ.

We substitute the similarity forms (13), (D1) and (D2) into the system (11), and ignore diffusion as it cannot produce any finite time singularity. The ϵ-equation gives,

$$
\begin{aligned}
\frac{B_0}{(t_0-t)^{1+q}}\left(q\,E+r\,\xi\,E'\right) = {} & 2\,\chi(\rho_a^0)\left(\zeta_{\rm avg}\,\frac{C_0}{(t_0-t)^{s+2r}}R''+\zeta_{\rm rel}\,\frac{A_0}{(t_0-t)^{p+2r}}\Phi''\right)\\
& +\left(B-C^2\right)\frac{B_0}{(t_0-t)^{q+2r}}E''-2\,\chi'(\rho_a^0)\,C\left(\zeta_{\rm avg}\,\frac{C_0}{(t_0-t)^{s}}R+\zeta_{\rm rel}\,\frac{A_0}{(t_0-t)^{p}}\Phi\right)\frac{B_0}{(t_0-t)^{q+2r}}E''\\
& -2\,\chi'(\rho_a^0)\,C\left(\zeta_{\rm avg}\,\frac{C_0}{(t_0-t)^{s+r}}R'+\zeta_{\rm rel}\,\frac{A_0}{(t_0-t)^{p+r}}\Phi'\right)\frac{B_0}{(t_0-t)^{q+r}}E'\\
& -2\,\chi'(\rho_a^0)\,C\left(\zeta_{\rm avg}\,\frac{C_0}{(t_0-t)^{s+r}}R'+\zeta_{\rm rel}\,\frac{A_0}{(t_0-t)^{p+r}}\Phi'\right)\frac{B_0}{(t_0-t)^{q+r}}E'\\
& -2\,\chi'(\rho_a^0)\,C\left(\zeta_{\rm avg}\,\frac{C_0}{(t_0-t)^{s+2r}}R''+\zeta_{\rm rel}\,\frac{A_0}{(t_0-t)^{p+2r}}\Phi''\right)\frac{B_0}{(t_0-t)^{q}}E\\
& +2\chi''(\rho_a^0)\,C^2\left(\zeta_{\rm avg}\,\frac{C_0}{(t_0-t)^{s+r}}R'+\zeta_{\rm rel}\,\frac{A_0}{(t_0-t)^{p+r}}\Phi'\right)\frac{B_0^2}{(t_0-t)^{2q+r}}EE'\\
& +\chi''(\rho_a^0)\,C^2\left(\zeta_{\rm avg}\,\frac{C_0}{(t_0-t)^{s+2r}}R''+\zeta_{\rm rel}\,\frac{A_0}{(t_0-t)^{p+2r}}\Phi''\right)\frac{B_0^2}{(t_0-t)^{2q}}E^2\\
& +2\chi''(\rho_a^0)\,C^2\left(\zeta_{\rm avg}\,\frac{C_0}{(t_0-t)^{s}}R+\zeta_{\rm rel}\,\frac{A_0}{(t_0-t)^{p}}\Phi\right)\frac{B_0^2}{(t_0-t)^{2q+2r}}\left(EE''+E'^2\right)\\
& +2\chi''(\rho_a^0)\,C^2\left(\zeta_{\rm avg}\,\frac{C_0}{(t_0-t)^{s+r}}R'+\zeta_{\rm rel}\,\frac{A_0}{(t_0-t)^{p+r}}\Phi'\right)\frac{B_0^2}{(t_0-t)^{2q+r}}EE'. \qquad \text{(D3)}
\end{aligned}
$$

The ρ-equation gives,

$$
\begin{aligned}
\frac{C_0}{(t_0-t)^{1+s}}\left(s\,R+r\,\xi\,R'\right) = &-\frac{C_0}{(t_0-t)^{s+r}}R'\times \\
&\Bigg[2\,\chi(\rho_a^0)\left(\zeta_{\rm avg}\,\frac{C_0}{(t_0-t)^{s+r}}R'+\zeta_{\rm rel}\,\frac{A_0}{(t_0-t)^{p+r}}\Phi'\right) \\
&+\left(B-C^2\right)\frac{B_0}{(t_0-t)^{q+r}}E'-2\,\chi'(\rho_a^0)\,C\left(\zeta_{\rm avg}\,\frac{C_0}{(t_0-t)^{s}}R+\zeta_{\rm rel}\,\frac{A_0}{(t_0-t)^{p}}\Phi\right)\frac{B_0}{(t_0-t)^{q+r}}E' \\
&-2\,\chi'(\rho_a^0)\,C\left(\zeta_{\rm avg}\,\frac{C_0}{(t_0-t)^{s+r}}R'+\zeta_{\rm rel}\,\frac{A_0}{(t_0-t)^{p+r}}\Phi'\right)\frac{B_0}{(t_0-t)^{q}}E \\
&+2\chi''(\rho_a^0)\,C^2\left(\zeta_{\rm avg}\,\frac{C_0}{(t_0-t)^{s}}R+\zeta_{\rm rel}\,\frac{A_0}{(t_0-t)^{p}}\Phi\right)\frac{B_0^2}{(t_0-t)^{2q+r}}EE' \\
&+\chi''(\rho_a^0)\,C^2\left(\zeta_{\rm avg}\,\frac{C_0}{(t_0-t)^{s+r}}R'+\zeta_{\rm rel}\,\frac{A_0}{(t_0-t)^{p+r}}\Phi'\right)\frac{B_0^2}{(t_0-t)^{2q}}E^2\Bigg] \\
&-\frac{C_0}{(t_0-t)^{s}}R\times \\
&\Bigg[2\,\chi(\rho_a^0)\left(\zeta_{\rm avg}\,\frac{C_0}{(t_0-t)^{s+2r}}R''+\zeta_{\rm rel}\,\frac{A_0}{(t_0-t)^{p+2r}}\Phi''\right) \\
&+\left(B-C^2\right)\frac{B_0}{(t_0-t)^{q+2r}}E''-2\,\chi'(\rho_a^0)\,C\left(\zeta_{\rm avg}\,\frac{C_0}{(t_0-t)^{s}}R+\zeta_{\rm rel}\,\frac{A_0}{(t_0-t)^{p}}\Phi\right)\frac{B_0}{(t_0-t)^{q+2r}}E'' \\
&-2\,\chi'(\rho_a^0)\,C\left(\zeta_{\rm avg}\,\frac{C_0}{(t_0-t)^{s+r}}R'+\zeta_{\rm rel}\,\frac{A_0}{(t_0-t)^{p+r}}\Phi'\right)\frac{B_0}{(t_0-t)^{q+r}}E' \\
&-2\,\chi'(\rho_a^0)\,C\left(\zeta_{\rm avg}\,\frac{C_0}{(t_0-t)^{s+r}}R'+\zeta_{\rm rel}\,\frac{A_0}{(t_0-t)^{p+r}}\Phi'\right)\frac{B_0}{(t_0-t)^{q+r}}E' \\
&-2\,\chi'(\rho_a^0)\,C\left(\zeta_{\rm avg}\,\frac{C_0}{(t_0-t)^{s+2r}}R''+\zeta_{\rm rel}\,\frac{A_0}{(t_0-t)^{p+2r}}\Phi''\right)\frac{B_0}{(t_0-t)^{q}}E \\
&+2\chi''(\rho_a^0)\,C^2\left(\zeta_{\rm avg}\,\frac{C_0}{(t_0-t)^{s+r}}R'+\zeta_{\rm rel}\,\frac{A_0}{(t_0-t)^{p+r}}\Phi'\right)\frac{B_0^2}{(t_0-t)^{2q+r}}EE' \\
&+\chi''(\rho_a^0)\,C^2\left(\zeta_{\rm avg}\,\frac{C_0}{(t_0-t)^{s+2r}}R''+\zeta_{\rm rel}\,\frac{A_0}{(t_0-t)^{p+2r}}\Phi''\right)\frac{B_0^2}{(t_0-t)^{2q}}E^2 \\
&+2\chi''(\rho_a^0)\,C^2\left(\zeta_{\rm avg}\,\frac{C_0}{(t_0-t)^{s}}R+\zeta_{\rm rel}\,\frac{A_0}{(t_0-t)^{p}}\Phi\right)\frac{B_0^2}{(t_0-t)^{2q+2r}}\left(EE''+E'^2\right) \\
&+2\chi''(\rho_a^0)\,C^2\left(\zeta_{\rm avg}\,\frac{C_0}{(t_0-t)^{s+r}}R'+\zeta_{\rm rel}\,\frac{A_0}{(t_0-t)^{p+r}}\Phi'\right)\frac{B_0^2}{(t_0-t)^{2q+r}}EE'\Bigg]. \qquad \text{(D4)}
\end{aligned}
$$

The ϕ-equation gives,

$$
\begin{aligned}
\frac{A_0}{(t_0-t)^{1+p}}\Big(p\,\Phi + r\,\xi\,\Phi'\Big) = &-\frac{A_0}{(t_0-t)^{p+r}}\Phi' \times \\
&\Bigg[2\,\chi(\rho_a^0)\left(\zeta_{\rm avg}\,\frac{C_0}{(t_0-t)^{s+r}}R' + \zeta_{\rm rel}\,\frac{A_0}{(t_0-t)^{p+r}}\Phi'\right) \\
&+\big(B-C^2\big)\frac{B_0}{(t_0-t)^{q+r}}E' - 2\,\chi'(\rho_a^0)\,C\left(\zeta_{\rm avg}\,\frac{C_0}{(t_0-t)^{s}}R + \zeta_{\rm rel}\,\frac{A_0}{(t_0-t)^{p}}\Phi\right)\frac{B_0}{(t_0-t)^{q+r}}E' \\
&-2\,\chi'(\rho_a^0)\,C\left(\zeta_{\rm avg}\,\frac{C_0}{(t_0-t)^{s+r}}R' + \zeta_{\rm rel}\,\frac{A_0}{(t_0-t)^{p+r}}\Phi'\right)\frac{B_0}{(t_0-t)^{q}}E \\
&+2\chi''(\rho_a^0)\,C^2\left(\zeta_{\rm avg}\,\frac{C_0}{(t_0-t)^{s}}R + \zeta_{\rm rel}\,\frac{A_0}{(t_0-t)^{p}}\Phi\right)\frac{B_0^2}{(t_0-t)^{2q+r}}EE' \\
&+\chi''(\rho_a^0)\,C^2\left(\zeta_{\rm avg}\,\frac{C_0}{(t_0-t)^{s+r}}R' + \zeta_{\rm rel}\,\frac{A_0}{(t_0-t)^{p+r}}\Phi'\right)\frac{B_0^2}{(t_0-t)^{2q}}E^2\Bigg] \\
&-\frac{A_0}{(t_0-t)^{p}}\Phi \times \\
&\Bigg[2\,\chi(\rho_a^0)\left(\zeta_{\rm avg}\,\frac{C_0}{(t_0-t)^{s+2r}}R'' + \zeta_{\rm rel}\,\frac{A_0}{(t_0-t)^{p+2r}}\Phi''\right) \\
&+\big(B-C^2\big)\frac{B_0}{(t_0-t)^{q+2r}}E'' - 2\,\chi'(\rho_a^0)\,C\left(\zeta_{\rm avg}\,\frac{C_0}{(t_0-t)^{s}}R + \zeta_{\rm rel}\,\frac{A_0}{(t_0-t)^{p}}\Phi\right)\frac{B_0}{(t_0-t)^{q+2r}}E'' \\
&-2\,\chi'(\rho_a^0)\,C\left(\zeta_{\rm avg}\,\frac{C_0}{(t_0-t)^{s+r}}R' + \zeta_{\rm rel}\,\frac{A_0}{(t_0-t)^{p+r}}\Phi'\right)\frac{B_0}{(t_0-t)^{q+r}}E' \\
&-2\,\chi'(\rho_a^0)\,C\left(\zeta_{\rm avg}\,\frac{C_0}{(t_0-t)^{s+r}}R' + \zeta_{\rm rel}\,\frac{A_0}{(t_0-t)^{p+r}}\Phi'\right)\frac{B_0}{(t_0-t)^{q+r}}E' \\
&-2\,\chi'(\rho_a^0)\,C\left(\zeta_{\rm avg}\,\frac{C_0}{(t_0-t)^{s+2r}}R'' + \zeta_{\rm rel}\,\frac{A_0}{(t_0-t)^{p+2r}}\Phi''\right)\frac{B_0}{(t_0-t)^{q}}E \\
&+2\chi''(\rho_a^0)\,C^2\left(\zeta_{\rm avg}\,\frac{C_0}{(t_0-t)^{s+r}}R' + \zeta_{\rm rel}\,\frac{A_0}{(t_0-t)^{p+r}}\Phi'\right)\frac{B_0^2}{(t_0-t)^{2q+r}}EE' \\
&+\chi''(\rho_a^0)\,C^2\left(\zeta_{\rm avg}\,\frac{C_0}{(t_0-t)^{s+2r}}R'' + \zeta_{\rm rel}\,\frac{A_0}{(t_0-t)^{p+2r}}\Phi''\right)\frac{B_0^2}{(t_0-t)^{2q}}E^2 \\
&+2\chi''(\rho_a^0)\,C^2\left(\zeta_{\rm avg}\,\frac{C_0}{(t_0-t)^{s}}R + \zeta_{\rm rel}\,\frac{A_0}{(t_0-t)^{p}}\Phi\right)\frac{B_0^2}{(t_0-t)^{2q+2r}}\Big(EE'' + E'^2\Big) \\
&+2\chi''(\rho_a^0)\,C^2\left(\zeta_{\rm avg}\,\frac{C_0}{(t_0-t)^{s+r}}R' + \zeta_{\rm rel}\,\frac{A_0}{(t_0-t)^{p+r}}\Phi'\right)\frac{B_0^2}{(t_0-t)^{2q+r}}EE'\Bigg]. \qquad \text{(D5)}
\end{aligned}
$$

Then by balancing the powers of (t_0-t) on the LHS and χ'' terms on the RHS, equations (15) in the main text are obtained.

Appendix E: Movie Captions

E1. Segregation of a binary mixture of stresslets with density peak co-localization

Movie 1. This movie shows segregation, followed by the formation of singularities in the profiles of ρ and ϕ and ϵ of the stresslets, where the density peaks co-localize. Initial conditions are homogeneous unstrained state with noise. Both stresslets are of catch bond type. Parameters set at $B = 6$, $C = 1$, $D = 1$, $k_1 = 1$, $k_2 = 0$, $k^b_{\rm rel} = 0$, $\zeta_{avg} = 2$, $\zeta_{rel} = 2$, $\alpha_1 = 4.5$,$\alpha_2 = 0.5$, $\chi(\rho_a^0) = 1$, $\chi'(\rho_a^0) = 1$, $\chi''(\rho_a^0) = 0.5$, $\chi'''(\rho_a^0) = -10$, $\eta = 10$, $K =$

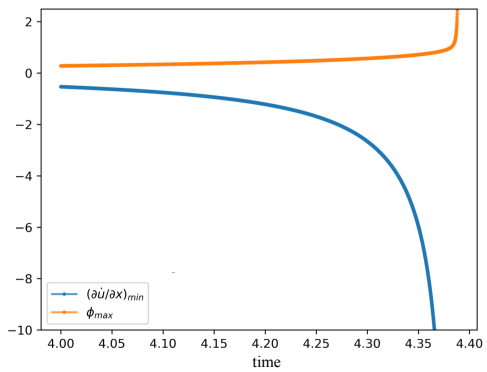

FIG. D8. Strain rate $\dot{\epsilon}$ blows up faster than the segregation field ϕ, as the singularity is approached.

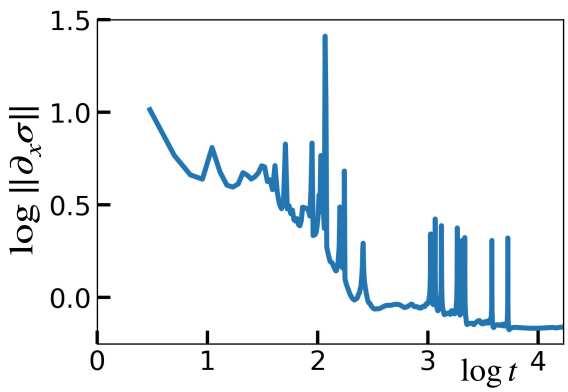

FIG. D9. Log of L^2 norm of $\partial_x \sigma$, $\|\partial_x \sigma\| := \sqrt{\int |\partial_x \sigma|^2 dx}$, is plotted as a function of log time, in the case where the two myosin species have catch bonds (Movie S4). The stress gradient shows an overall decrease in time, except at isolated time points associated with the onset of singularity mergers. This could be interpreted as a Lyapunov functional, if smoothened with a suitable mollifier.

0.5, $L = 32$.

E2. Segregation of a binary mixture of stresslets with density peak separation

Movie 2. This movie shows segregation, followed by the formation of singularities in the profiles of ρ and ϕ and ϵ of the stresslets, where the density peaks separate. Initial conditions are homogeneous unstrained state with noise. One stresslet is of a catch bond type and the other is of a slip bond type. Parameters are set at $B = 6$, $C = 1$, $D = 1$, $k_1 = 1$, $k_2 = 0$, $k^b_{\rm rel} = 0$, $\zeta_{avg} = 2$, $\zeta_{rel} = 2$, $\alpha_1 = 0.5$,$\alpha_2 = -3.5$, $\chi(\rho^0_a) = 1$, $\chi'(\rho^0_a) = 1$, $\chi''(\rho^0_a) = 0.5$, $\chi'''(\rho^0_a) = -10$, $\eta = 10$, $K = 0.5$.

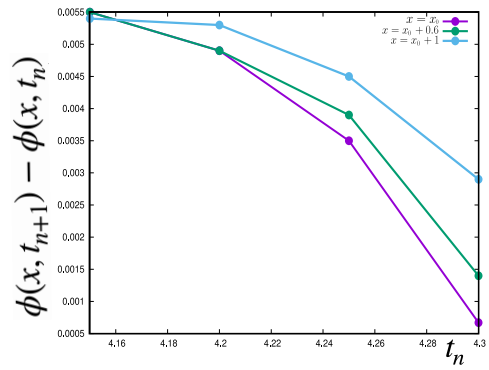

FIG. D10. Cauchy convergence of $\phi(x, t)$ in time t as the singularity is approached; points closer to the blow-up location x_0 diverge faster.

E3. Dynamics of singularity formation

Movie 3. This movie (left panel) shows the approach to a finite time elastic singularity, and (right panel) shows its physical resolution by a steric term ($B_3 \neq 0$) . Parameters are set at $B = 6$, $C = 1$, $D = 1$, $k_1 = 1$, $k_2 = 0$, $k^b_{\rm rel} = 0$, $\zeta_{avg} = 2$, $\zeta_{rel} = 2$, $\alpha_1 = 4$,$\alpha_2 = 0$, $\chi(\rho^0_a) = 1$, $\chi'(\rho^0_a) = 1$, $\chi''(\rho^0_a) = 0.5$, $\chi'''(\rho^0_a) = 0$ (for left panel), $\chi'''(\rho^0_a) = -10$ (for right panel), $\eta = 10$, $K = 0.1$, $L = 10$.

E4. Coarsening Dynamics: catch bond with turnover

Movie 4. This movie shows the coarsening dynamics of elastic singularities, in a system where both stresslets have catch bonds. At first, the singularities merge quickly following which the coarsening slows down, showing signs of dynamical arrest. Parameters are set at $B = 5$, $C = 1$, $D = 1$, $k_1 = 1$, $k_2 = 0$, $k^b_{\rm rel} = 0$, $\zeta_{avg} = 1.4$, $\zeta_{rel} = 1$, $\alpha_1 = 3$,$\alpha_2 = 1$, $\chi(\rho^0_a) = 1$, $\chi'(\rho^0_a) = 1$, $\chi''(\rho^0_a) = 0.5$, $\chi'''(\rho^0_a) = -15$, $\eta = 0.5$, $K = 0.01$, $L = 600$.

E5. Coarsening Dynamics: catch bond without turnover

Movie 5. The configurations generated in the previous numerical simulation of coarsening dynamics of the species with catch bonds at $t = 100$, is further evolved without turnover. The singularities broaden and merge faster in the absence of turnover and even undergo splitting on occasion. Parameters are set at $B = 5$, $C = 1$,

$D = 1.5$, $k_1 = 1$, $k_2 = 0$, $k^b_{\rm rel} = 0$, $\zeta_{avg} = 1.4$, $\zeta_{rel} = 1$, $\chi(\rho^0_a) = 1$, $\chi'(\rho^0_a) = 1$, $\chi''(\rho^0_a) = 0.5$, $\chi'''(\rho^0_a) = -15$, $\eta = 25$, $K = 10$, $L = 600$.

E6. Coarsening Dynamics: slip bond with turnover

Movie 6. This movie shows the coarsening dynamics of the singularities where one stresslet has a catch bond and the other, a slip bond. Parameters are set at $B = 5$, $C = 1$, $D = 1$, $k_1 = 1$, $k_2 = 0$, $k^b_{\rm rel} = 0$, $\zeta_{avg} = 1.4$, $\zeta_{rel} = 1$, $\alpha_1 = 0.5$,$\alpha_2 = -1.5$, $\chi(\rho^0_a) = 1$, $\chi'(\rho^0_a) = 1$, $\chi''(\rho^0_a) = 0.5$, $\chi'''(\rho^0_a) = -10$, $\eta = 0.5$, $K = 0.01$, $L = 600$.

E7. Travelling wave state

Movie 7. This movie shows an initial standing wave which transitions to a travelling wave at steady state. Parameters are set at $B = 5$, $C = 1$, $D = 1$, $k_1 = 1$, $k_2 = 0$, $k^b_{\rm rel} = 0$, $\zeta_{avg} = 2.8$, $\zeta_{rel} = 1$, $\alpha_1 = -3$,$\alpha_2 = -5$, $\chi(\rho^0_a) = 1$, $\chi'(\rho^0_a) = 1$, $\chi''(\rho^0_a) = 0.1$, $\chi'''(\rho^0_a) = -15$, $\eta = 0.1$, $K = 1$, $L = 64$.

E8. Swap state

Movie 8. This movie shows a standing wave (swap) steady state following an initial transient. Parameters are set at $B = 5$, $C = 1$, $D = 1$, $k_1 = 1$, $k_2 = 0$, $k^b_{\rm rel} = 0$, $\zeta_{avg} = 2.2$, $\zeta_{rel} = 1$, $\alpha_1 = -9$,$\alpha_2 = -11$, $\chi(\rho^0_a) = 1$, $\chi'(\rho^0_a) = 1$, $\chi''(\rho^0_a) = 0.1$, $\chi'''(\rho^0_a) = -15$, $\eta = 0.1$, $K = 1$, $L = 64$.

E9. Peristalsis

Movie 9. This movie shows a pulse sluggishly travelling on a segregated profile. Parameters are set at $B = 5$, $C = 1$, $D = 1$, $k_1 = 1$, $k_2 = 0$, $k^b_{\rm rel} = 0$, $\zeta_{avg} = 3$, $\zeta_{rel} = 1$, $\alpha_1 = 0.03$,$\alpha_2 = -2.03$, $\chi(\rho^0_a) = 1$, $\chi'(\rho^0_a) = 1$, $\chi''(\rho^0_a) = 0.1$, $\chi'''(\rho^0_a) = -15$, $\eta = 0.1$, $K = 1$, $L = 64$.

E10. Coexistence of nonequilibrium phases

Movie 10. This movie shows how an initial standing wave starts to travel while pulsing. This undulating travelling wave persists for a very long time, eventually transitioning to static segregated configuration. Parameters are set at $B = 6$, $C = 1$, $D = 1$, $k_1 = 1$, $k_2 = 0$, $k^b_{\rm rel} = 0$, $\zeta_{avg} = 2$, $\zeta_{rel} = -1.789$, $\alpha_1 = 4.989$,$\alpha_2 = -0.989$, $\chi(\rho^0_a) = 1$, $\chi'(\rho^0_a) = 1$, $\chi''(\rho^0_a) = 0.1$, $\chi'''(\rho^0_a) = -15$, $\eta = 0.5$, $K = 1$, $L = 64$.

The pseudospectral code and the analysis notebook used to create the Movies 1-10 can be accessed here.

[1] T. D. Pollard and R. D. Goldman (Editors), *The Cytoskeleton*, Cold Spring Harbor Laboratory Press (2016).

[2] P. Hotulainen and P. Lappalainen, *Stress fibers are generated by two distinct actin assembly mechanisms in motile cells*, The Journal of Cell Biology **173**, 383–394 (2006).

[3] J. I. Lehtimäki, E. K. Rajakylä, S. Tojkander and Pekka Lappalainen, *Generation of stress fibers through myosin-driven re-organization of the actin cortex*, eLife **10**, e60710 (2021).

[4] A. Roychowdhury, M. Rao and L. Truskinovsky, *Active drive towards elastic spinodals*, arXiv:2403.17517 (2024).

[5] T. Vignaud, C. Copos, C. Leterrier, M. Toro-Nahuelpan, Q. Tseng , J. Mahamid, L. Blanchoin, A. Mogilner, M. Théry and L. Kurzawa, *Stress fibres are embedded in a contractile cortical network*, Nature Materials **20**, 410–420 (2021).

[6] M. Kovács, K. Thirumurugan, P. J. Knight, and J. R. Sellers, *Load-dependent mechanism of nonmuscle myosin 2*, The Proceedings of the National Academy of Sciences **104**, 9994–9999 (2007).

[7] R. Fernandez-Gonzalez, S. M. Simoes, J-C Röper, S. Eaton, and J. A. Zallen, *Myosin II dynamics are regulated by tension in intercalating cells*, Developmental Cell **17**, 736–743 (2009)

[8] Y. Mulla, M. J. Avellaneda, A. Roland, L. Baldauf, S. J. Tans and G. H. Koenderink, *Weak catch bonds make strong networks*, Nature Materials **21**, 1019–1023 (2022).

[9] R. J. Hawkins and T. B. Liverpool, *Stress Reorganisation and Response in Active Solids*, Physical Review Letters **113**, 028102 (2014).

[10] T. Hiraiwa and G. Salbreux, *Role of Turnover in Active Stress Generation in a Filament Network*, Physical

Review Letters **116**, 188101 (2016).

[11] K. L. Weirich, S. Stam, E. Munro and M. L. Gardel, *Actin bundle architecture and mechanics regulate myosin II force generation*, Biophysical Journal **120**, 1957-1970 (2021).

[12] S. Hu, K. Dasbiswas, Z. Guo, Y-H. Tee, V. Thiagarajan, P. Hersen, T-L. Chew, S. A. Safran, R. Zaidel-Bar, and A. D. Bershadsky, *Long-range self-organization of cytoskeletal myosin II filament stacks*, Nature Cell Biology **19**, 133–141 (2017).

[13] W. Luo, C.-han Yu, Z. Z. Lieu, J. Allard, A. Mogilner, M. P. Sheetz, A. D. Bershadsky, *Analysis of the local organization and dynamics of cellular actin networks*, Journal of Cell Biology **202**, 1057–1073 (2013).

[14] K. Weißenbruch, J. Grewe, M. Hippler, M. Fladung, M. Tremmel, K. Stricker, U. S. Schwarz and M. Bastmeyer, *Distinct roles of nonmuscle myosin II isoforms for establishing tension and elasticity during cell morphodynamics*, eLife **10**, e71888 (2021).

[15] J. R. Beach, L. Shao, K. Remmert, D. Li, E. Betzig and J. A. Hammer III, *Nonmuscle Myosin II Isoforms Coassemble in Living Cells*, Current Biology **24**, 1160–1166 (2014).

[16] R. Fernandez-Gonzalez, and J.A. Zallen, *Oscillatory behaviors and hierarchical assembly of contractile structures in intercalating cells*, Physical Biology **8**, 045005 (2011).

[17] A. Munjal, J-M. Philippe, E. Munro and T. Lecuit, *A self-organized biomechanical network drives shape changes during tissue morphogenesis*, Nature **524**, 351–355 (2015).

[18] D. S. Banerjee, A. Munjal, T. Lecuit and M. Rao, *Actomyosin pulsation and flows in an active elastomer with turnover and network remodeling*, Nature Communications **8**, 1121 (2017).

[19] K. Dierkes, A. Sumi, J. Solon and G. Salbreux, *Spontaneous oscillations of elastic contractile materials with turnover*, Physical Review Letters **113**, 148102 (2014).

[20] M. C. Marchetti, J.-F. Joanny, S. Ramaswamy, T. B. Liverpool, J. Prost, M. Rao and R.A. Simha, *Hydrodynamics of Soft Active Matter*, Review of Modern Physics **85**, 1143–1189 (2013).

[21] M. S. Shutova, S. B. Asokan, S. Talwar, R. K. Assoian, J. E. Bear and T. M. Svitkina, *Self-sorting of nonmuscle myosins IIA and IIB polarizes the cytoskeleton and modulates cell motility*, Journal of Cell Biology **216**, 2877–2889 (2017).

[22] K. Weißenbruch, M. Fladung, J. Grewe, L. Baulesch, U. S. Schwarz and M. Bastmeyer, *Nonmuscle myosin IIA dynamically guides regulatory light chain phosphorylation and assembly of nonmuscle myosin IIB*, European Journal of Cell Biology **101**, 151213 (2022).

[23] S. Banerjee, T.B. Liverpool and M.C. Marchetti, *Generic phases of cross-linked active gels: Relaxation, oscillation and contractility*, Europhysics Letters **96**, 58004 (2011).

[24] S. Banerjee and M.C. Marchetti, *Instabilities and oscillations in isotropic active gels*, Soft Matter **7**, 463 (2011).

[25] Abhishek M., A. Dhanuka, D. S. Banerjee and M. Rao, *Nonlinear excitability of an renewable active elastomer*, in preparation.

[26] A. J. Bray, *Theory of phase ordering kinetics*, Advances in Physics **51**, 481–587 (2002).

[27] J. Eggers and M. A. Fontelos, *Singularities: Formation, Structure, and Propagation*, Cambridge University Press, Cambridge, UK (2015).

[28] P. Ronceray, C. P. Boedersz and M. Lenz, *Fiber networks amplify active stress*, The Proceedings of the National Academy of Sciences **113**, 2827–2832 (2016).

[29] M. Fruchart, R. Hanai, P. B. Littlewood, and V. Vitelli, *Non-reciprocal phase transitions*, Nature **592**, 363–369 (2021).

[30] T. Kato, *Perturbation Theory for Linear Operators*, 2nd edn, Springer (1984).

[31] Z. You, A. Baskaran and M. C. Marchetti, *Nonreciprocity as a generic route to traveling states*, The Proceedings of the National Academy of Sciences **117**, 19767–19772 (2020).

[32] M. P. Murrell and M. L. Gardel, *F-actin buckling coordinates contractility and severing in a biomimetic actomyosin cortex*, Proceedings of the National Academy of Sciences **109**, 20820–20825 (2012).

[33] P. Müller and J. Kierfeld, *Wrinkling of random and regular semiflexible polymer networks*, Physical Review Letters **112**, 094303 (2014).

[34] O. U. Salman, G. Vitale and L. Truskinovsky, *Continuum theory of bending-to-stretching transition*, Physical Review E **100**, 051001 (2019).

[35] K. J. Burns, G. M. Vasil, J. S. Oishi, D. Lecoanet and B. P. Brown, *Dedalus: A Flexible Framework for Numerical Simulations with Spectral Methods*, Physical Review Research **2**, 023068 (2020).

[36] D. Wang, S. J. Ruuth, *Variable Step-Size Implicit-Explicit Linear Multistep Methods for Time-Dependent Partial Differential Equations*, Journal of Computational Mathematics **26**, 6, 838-855 (2008).

[37] V. I. Arnold, S. F. Shandarin and Ya. B. Zel'dovich, *The Large Scale Structure of the Universe I. General Properties. One and Two Dimensional Models*, Geophysical and Astrophysical Fluid Dynamics **20**, 111-130 (1982).

[38] J. Feldbrugge, R. van de Weygaert, J. Hidding and J. Feldbrugge, *Caustic skeleton and cosmic web*, Journal of Cosmology and Astroparticle Physics **2018**, 27 (2018).

[39] V. I. Arnold, S. M. Gusein-Zade and A. N. Varchenko, *Singularities of Differentiable Maps, Vol. 1*, Birkhäuser (1988).

[40] R. Abeyaratne and J. K. Knowles, *Kinetic relations and the propagation of phase boundaries in solids*, Archive for Rational Mechanics and Analysis **114**, 119-154 (1991).

[41] A. Roychowdhury, S. Dasgupta and M. Rao, *Emergence of Tension Chains and Active Force Patterning*, arXiv:2206.06770.

[42] J. P. Banerjee, R. Mandal, D. S. Banerjee, S. Thutupalli and M. Rao, *Unjamming and emergent nonreciprocity in active ploughing through a compressible viscoelastic fluid*, Nature Communications **13**, 4533 (2022).

[43] R. K. Gupta, R. Kant, H. Soni, A. K. Sood and S. Ramaswamy, *Active nonreciprocal attraction between motile particles in an elastic medium*, Physical Review E **105**, 064602 (2022).

[44] J. R. Beach, et al. *Actin dynamics and competition for myosin monomer govern the sequential amplification of myosin filaments*, Nature Cell Biology **19**, 85–93 (2017).

[45] L. N. Trefethen, A. E. Trefethen, S. C. Reddy and T A Driscoll, *Hydrodynamic Stability Without Eigenvalues*, Science **261**, 578–584 (1993).

[46] L. N. Trefethen and M. Embree, *Spectra and Pseudospectra*, Princeton University Press (2005).

[47] M. Stern and A. Murugan, *Learning Without Neurons in*

Physical Systems, Annual Review of Condensed Matter Physics **14**, 417–441 (2023).

[48] S. Banerjee, M. L. Gardel and U. S. Schwarz, *The actin cytoskeleton as an active adaptive material*, Annual Review of Condensed Matter Physics **11**, 421–439 (2020).

[49] D. E. Ingber, N. Wang and D. Stamenović, *Tensegrity, cellular biophysics, and the mechanics of living systems*, Reports on Progress in Physics **77**, 046603 (2014).

[50] M. Vicente-Manzanares, M. A. Koach, L. Whitmore, M. L. Lamers and A. F. Horwitz, *Segregation and activation of myosin IIB creates a rear in migrating cells*, Journal of Cell Biology **183**, 543–554 (2008).

[51] A. J. Jimenez, A. Schaeffer, C. D. Pascalis, G. Letort, B. Vianay, M. Bornens, M. Piel, L. Blanchoin and M. Théry, *Acto-myosin network geometry defines centrosome position*, Current Biology **31**, 1206–1220 (2021).

[52] R. Zhang, S. A. Redford, P. V. Ruijgrok, N. Kumar, A. Mozaffari, S. Zemsky, A. R. Dinner, V. Vitelli, Z. Bryant, M. L. Gardel and J. J. de Pablo, *Spatiotemporal control of liquid crystal structure and dynamics through activity patterning*, Nature Materials **20**, 875–882 (2021).